UNIVERSITY OF OKLAHOMA

GRADUATE COLLEGE

SUBSEASONAL VARIABILITY OF BIOMASS BURNING AEROSOL RADIATIVE PROPERTIES RETRIEVED BY 4STAR DURING THE ORACLES 2016-2018 CAMPAIGNS

A THESIS

SUBMITTED TO THE GRADUATE FACULTY

in partial fulfillment of the requirements for the

Degree of

MASTER OF SCIENCE IN METEOROLOGY

By

LOGAN MITCHELL
Norman, Oklahoma
2022

Downloaded from SHAREOK. Persistent Handle URL: https://hdl.handle.net/11244/335508

SUBSEASONAL VARIABILITY OF BIOMASS BURNING AEROSOL RADIATIVE PROPERTIES RETRIEVED BY 4STAR DURING THE ORACLES 2016-2018 CAMPAIGNS

A THESIS APPROVED FOR THE
SCHOOL OF METEOROLOGY

BY THE COMMITTEE CONSISTING OF

Dr. Jens Redemann, Chair

Dr. Connor Flynn

Dr. Feng Xu

Dr. S. Marcela Loria-Salazar

© Copyright by LOGAN MITCHELL 2022
All rights reserved.

Table of Contents

List of Equations vi
List of Figures vii
List of Tables viii
Acknowledgements ix
Abstract x
Chapter 1 – Introduction 1
1.1 – What are Aerosols? 1
1.2 – Aerosol-Radiation Interactions 2
1.3 – Aerosol-Cloud Interactions 5
1.4 – Aerosol Types 6
1.5 – Aerosol Radiative Properties 8
1.6 – AERONET 11
1.7 – The Southeast Atlantic Ocean 12
1.8 – ORACLES 13
1.9 – The BB Emission Season 15
1.10 – Thesis Statement 17
Chapter 2 – Materials and Methods 18
2.1 – 4STAR 18
2.2 – AERONET Adapted Retrieval Code 20
2.3 – Wavelength Selection 30
2.4 – Quality Assurance/Quality Control 35
2.5 – AAE Calculation 46
2.6 – Subseasonal Analysis 47
Chapter 3 – Results 48
3.1 – SSA 48
3.2 – AOD 49
3.3 – AAOD 50
3.4 – Linear AAE 51
3.5 – Quadratic AAE 52

Chapter 4 – Discussion 53
4.1 – Subseasonal Variability of the Aerosol Radiative Properties 53
4.2 – ORACLES vs. AERONET 54
Chapter 5 – Conclusion 59
5.1 – Key Takeaways 59
5.2 – Future Work 61
5.3 – Environmental Implications 62
References 63

List of Equations

Equation 1.1 2
Equation 1.2 8
Equation 1.3 9
Equation 1.4 9
Equation 1.5 10
Equation 1.6 10

List of Figures

Figure 1.1 1
Figure 1.2 3
Figure 1.3 14
Figure 1.4 16
Figure 2.1 18
Figure 2.2 21
Figure 2.3 23
Figure 2.4 24
Figure 2.5 25
Figure 2.6 26
Figure 2.7 28
Figure 2.8 29
Figure 2.9 32
Figure 2.10 33
Figure 2.11 34
Figure 3.1 48
Figure 3.2 49
Figure 3.4 51
Figure 3.5 52
Figure 4.1 55
Figure 4.2 57

List of Tables

Table 2.1 36
Table 2.2 39
Table 2.3 43

Acknowledgements

Thanks to my committee chair, Dr. Jens Redemann, for his "big picture" advice and financial support that kept this thesis on track. Thanks to my second advisor, Dr. Connor Flynn, for his "small details" guidance that helped me conduct the analysis. Thanks to my other committee members, Dr. Feng Xu and Dr. Marcela Loria-Salazar, for their ideas regarding terminology, presentation, and future work. Thanks to Dr. Kristina Pistone for supplying data and code that made the continuation of ORACLES/4STAR analysis possible. Thanks to Dr. Samuel LeBlanc and Dr. Sebastian Schmidt for their feedback regarding conference presentations. Thanks to my OU and WKU professors for imparting the broad base of knowledge necessary to complete this thesis. Thanks to my family for their love and support. Thanks to my friends for keeping me sane during a global pandemic.

Abstract

Absorbing aerosols play a role in cloud and radiation processes, but these interactions are complex and have a high degree of uncertainty. The interactions of Biomass Burning (BB) aerosols with the semipermanent subtropical stratocumulus cloud deck over the Southeast Atlantic Ocean are reflected by large General Circulation Model (GCM) residuals in the region. Nearly two decades (1995-2013) of AERONET (AErosol RObotic NETwork) sun photometer measurements have documented an intense BB aerosol emission season from August to October, with subseasonal variations in aerosol scattering/absorption occurring in the source region of Southern Africa. During 2016-2018, NASA conducted the ORACLES (ObseRvations of Aerosols above CLouds and their intEractionS) airborne campaign to study BB aerosol-cloud-radiation interactions and BB aerosol transport above, within, and below the stratocumulus cloud deck over the Southeast Atlantic. ORACLES employed a 4STAR (Spectrometer for Sky-Scanning, Sun-Tracking Atmospheric Research) hyperspectral sun-sky spectrophotometer to measure solar radiation, including direct beam irradiances and sky radiances. The subseasonal variability of aerosol radiative properties retrieved from 4STAR during ORACLES is examined in the context of the extended AERONET record.

4STAR-retrieved aerosol radiative properties include Single Scattering Albedo (SSA), Aerosol Optical Depth (AOD), Aerosol Absorption Optical Depth (AAOD), and Absorption Ångström Exponent (AAE). SSA shows subseasonal variations in aerosol scattering and absorption, which is echoed by an analogous trend in AAOD. The subseasonal variation in SSA is large enough (0.04 - 0.06) that it can affect aerosol-induced radiative flux. The median AAE values (nominally 1) and small subseasonal variations indicate that aerosol type is dominated by spectrally uniform Black Carbon (BC), and that the subseasonal change in aerosol scattering/absorption is likely due to changes in BB aerosol composition. The subseasonal variations in SSA and AOD found during ORACLES over the SE Atlantic is in remarkable agreement with that of the extended AERONET record in Southern Africa, speaking to 4STAR's utility as a mobile, airborne AERONET-like platform.

Chapter 1 – Introduction

1.1 – What are Aerosols?

Aerosols are solid or liquid particles suspended in the atmosphere that can cause cooling or warming (Boucher et al., 2013), depending upon their properties and environmental factors. As such, aerosols perform important, yet complex, roles in both cloud and radiation physics (Zelinka et al., 2014). This is highlighted by the United Nation's IPCC (Intergovernmental Panel on Climate Change) AR6 (Sixth Assessment Report), released in 2021. Figure 1.1 shows how quantitative assessments of aerosol-cloud and aerosol-radiation interactions are still associated with high uncertainty (Forster et al., 2021), even though diligent work by atmospheric scientists has reduced uncertainty and constrained it within the net cooling direction since the release of the AR5 (Fifth Assessment Report) in 2013. Further reductions in aerosol uncertainties are critical to improving confidence in General Circulation Models (GCM), which are key to diagnosing and forecasting the effects of global climate change (Menon et al., 2002).

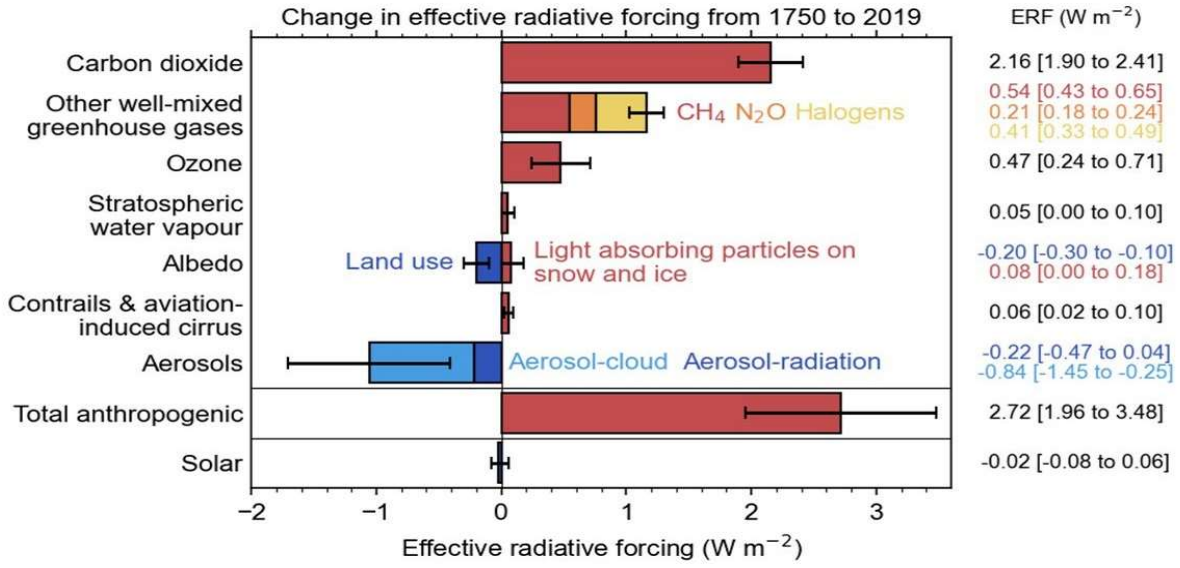

Figure 1.1 – Changes in global radiative forcing components. Adapted from Forster et al., 2021.

1.2 – Aerosol-Radiation Interactions

Radiant flux ($W = J \cdot s^{-1}$) is the rate of transfer of electromagnetic (EM) radiation. Irradiance ($W \cdot m^{-2}$) is the radiant flux received by the surface area of an object. Radiance ($W \cdot sr^{-1} \cdot m^{-2}$) is the irradiance of an object, per solid angle (Nicodemus, 1963). As such, radiance is directionally dependent, while irradiance is not. Irradiance can also be thought of as the integral of radiance over all angles. From the perspective of sun/sky photometers, direct solar irradiance is attributable to the discrete solar disk, while diffuse radiance is attributable to the extended sky.

Transmittance is the effectiveness of an object to allow EM radiation to pass through it. Radiation that is not transmitted is either absorbed or scattered (Yu et al., 2006). Absorption (Q_{abs}) is when a photon absorbs incident radiation, removing EM energy and heating the medium. Scattering (Q_{scat}) is when a photon reflects incident radiation, redirecting EM energy without local heating. Scattering Angle (SA) refers to the angle at which light is scattered. Extinction (Q_{ext}) is the total radiation that is absorbed or scattered by aerosols (Equation 1.1).

$$Q_{ext} = Q_{abs} + Q_{scat} \quad Equation\ 1.1$$

In general, aerosols are capable of absorbing or scattering light, which can result in either warming or cooling, respectively. The climatic effects of aerosols can be thought of in terms of Radiative Forcing (RF) and Effective Radiative Forcing (ERF). RF is the change in net radiative flux (downward minus upward) at the Top of Atmosphere (TOA) due to an imposed perturbation (Boucher et al., 2013). ERF is like RF, but holds certain surface conditions, such as global mean surface temperature, unchanged, such that ERF is instead sensitive to adjustments by aerosol-

impacted tropospheric variables, such as atmospheric temperature, cloud cover, and water vapor content (Zelinka et al., 2014). For aerosols, ERF is divided into ERFari (Effective Radiative Forcing from aerosol-radiation interactions) and ERFaci (Effective Radiative Forcing from aerosol-cloud interactions). ERFari (Figure 1.2) is composed of the direct effect, which is the primary RF, and the semi-direct effect, which acts as an RF adjustment.

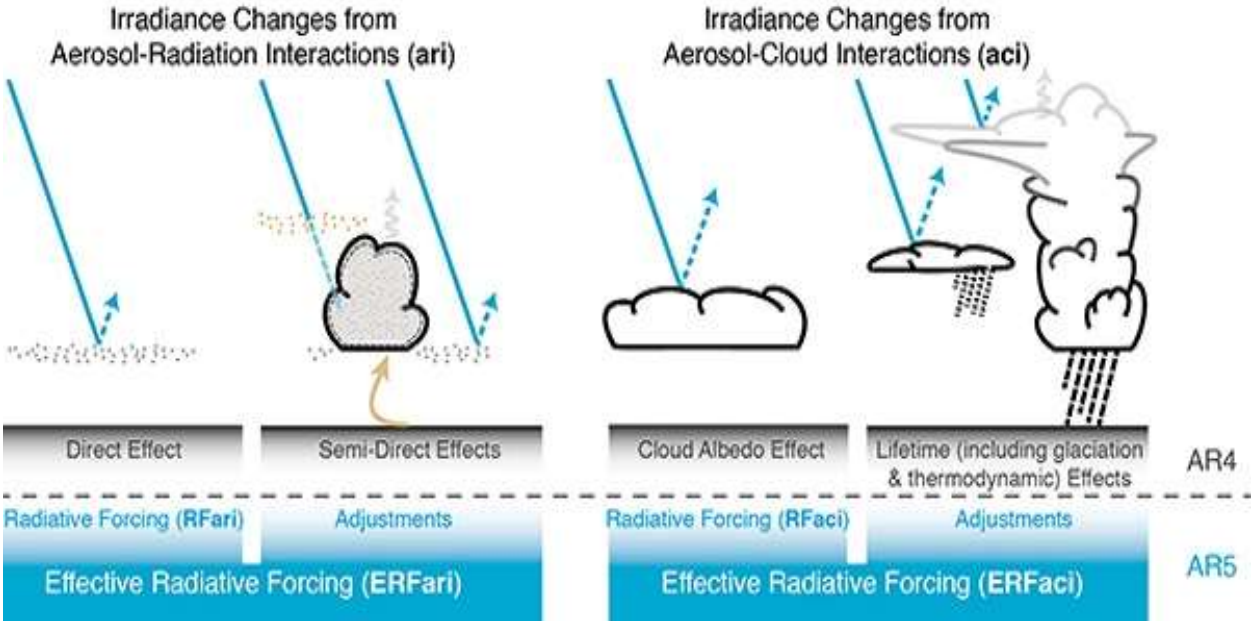

Figure 1.2 – Effective radiative forcing from aerosol-radiation interactions (left) and aerosol-cloud interactions (right). Adapted from Boucher et al., 2013.

The direct effect is a function of aerosol absorption and scattering (Charlson & Pilat, 1969). Aerosol absorption is a positive RF and results in effective warming. Aerosol scattering is a negative RF and results in effective cooling.

The semi-direct effect depends upon aerosol-induced warming of the atmosphere (Hansen et al., 1997). The aerosol-induced warming can create temperature inversions aloft that cap vertical cloud growth, stabilizing the atmosphere (Allen et al., 2019). The warming also

increases environmental temperature, which can reduce the local relative humidity below 100%, preventing the formation of new cloud droplets (Johnson et al., 2004). Heated absorbing aerosols can also evaporate bright edge-of-cloud droplets, exposing a darker background cloud albedo underneath (Wilcox, 2012). In all these scenarios, cloud cover is weakened, resulting in effective warming.

1.3 – Aerosol-Cloud Interactions

Aerosols are crucial to the formation of clouds. Extremely low temperatures are required to create cloud droplets via the homogeneous nucleation of pure water vapor, such that the process rarely occurs outside of lab conditions (Oxtoby, 1992). However, the simple addition of aerosols to serve as Cloud Condensation Nuclei (CCN) saves energy that would have been spent forming a cloud droplet nucleus, thus allowing heterogeneous nucleation to occur at warmer temperatures lower in the atmosphere (Andreae & Rosenfeld, 2008). This means that almost all cloud formation occurring in the troposphere is reliant upon the presence of aerosols (Liu, 2000).

ERFaci (Figure 1.2) is composed of the cloud albedo effect, which is the primary RF, and the lifetime effect, which serves as a RF adjustment. These two effects are also collectively known as the indirect effect. The cloud albedo effect occurs when clouds with a high concentration of aerosols form many small water droplets, "brightening" the cloud and increasing the reflection of incident radiation (Twomey, 1974). The lifetime effect is the ability of aerosols to extend cloud longevity by increasing the water content and maximum height achieved by clouds, with smaller droplets also simultaneously reducing the precipitation rate, all of which enables clouds to scatter more radiation during their prolonged lifetimes (Albrecht, 1989). The cloud albedo effect and the lifetime effect both increase radiation scattering by clouds, resulting in effective cooling.

1.4 – Aerosol Types

Absorbing aerosols are aerosols that absorb a fraction of incident light (Cappa et al., 2016). There are three major types of absorbing aerosols: black carbon, brown carbon, and mineral dust.

Black Carbon (BC) is an extremely dark aerosol that is a primary component in soot. Sources for BC include biomass burning, vehicular emissions, industrial processes, and power generation (Pósfai et al., 2004). BC is absorptive across the entire EM spectrum and thus has a uniform spectral dependence (Cappa et al., 2016). Absorption by BC aerosols can weaken marine stratocumulus cloud cover (Koch & Del Genio, 2010), resulting in effective warming.

Brown Carbon (BrC) is an aerosol that is lighter in coloration than BC. BrC is sourced almost exclusively from biomass burning but can also come about via secondary formation processes when BC is coated by organic and sulfate aerosols (Zhu et al., 2013). BrC is most absorptive in the short-visible and ultraviolet wavelengths (Cappa et al., 2016), with a strongly negative spectral dependence in this region. BrC was discovered much more recently than BC and thus its radiative forcings are not as well understood (Zhu et al., 2013). BC and BrC together comprise the absorbing component of Biomass Burning (BB) aerosols.

Mineral dust aerosols can have natural, rural, and urban sources, such as deserts (especially the Saharan Desert), agriculture, and construction, respectively. Common compositions of mineral dust aerosols include calcite, dolomite, feldspar, quartz, and clay minerals (Liu et al., 2019). Mineral dust aerosols are moderately absorptive in the long-visible and infrared wavelengths (Cappa et al., 2016), although the specifics depend on mineral composition.

Non-absorbing aerosols, on the other hand, are aerosols that do not absorb radiation (Stier et al., 2006). As such, they tend to have high albedo and are much lighter in coloration than absorbing aerosols. Common non-absorbing aerosols include sulfates (Kiehl & Briegleb, 1993), nitrates (Gibson et al., 2006), sea salt (Tang et al., 1997), pollen, and spores.

1.5 – Aerosol Radiative Properties

To classify absorbing aerosols by type, the radiative properties of the aerosols must first be determined and understood. Pertinent radiative properties include Single Scattering Albedo, Aerosol Optical Depth, Aerosol Absorption Optical Depth, and Absorption Ångström Exponent.

Single Scattering Albedo (SSA) is the ratio of scattering (Q_{scat}) to the total extinction (Q_{ext}) of a particle interacting with EM radiation (Equation 1.2). A value of unity implies total scattering, while a value of zero implies total absorption (Bergstrom et al., 2003). SSA is an intensive property of the aerosol, meaning that it is independent of aerosol loading and instead dependent upon the aerosol's physical and chemical characteristics, such as aerosol type, composition, morphology, age, and mixing state. Even a change in SSA of 0.05 can have a significant impact on the critical surface albedo, which is the inflection point between effective heating and effective cooling (Russell et al., 2002).

$$SSA = \frac{Q_{scat}}{Q_{ext}} \quad Equation\ 1.2$$

Aerosol Optical Depth (AOD) is the vertical columnar integral of extinction coefficient (α_{ext}) over height (z), from the surface to the TOA (Equation 1.3). Thus, the higher the AOD, the more radiation that is extinguished by aerosols (Bergstrom et al., 2003). AOD is an extensive property, meaning that it is dependent upon both aerosol type/composition and aerosol loading. In fact, since AOD is an extensive property and is focused on total aerosol extinction, it is often employed as a proxy for aerosol loading.

$$AOD = \int_{sfc}^{toa} \alpha_{ext}\, dz \;\; Equation\ 1.3$$

Aerosol extinction can be calculated for selected wavelengths via radiative transfer theory using complex refractive index and size distribution as input. Mie theory is one of the few exact solutions in radiative transfer theory that describes the radiative scattering of spherical particles that are similarly sized to the wavelength of the incident light. Mie theory is usually not employed for smaller particles (<1/10 of the incident wavelength) or larger particles, where it is more computationally efficient to instead use Rayleigh scattering (Souprayen et al., 1999) and geometric optics (Bi et al., 2009), respectively. However, typical atmospheric aerosols satisfy the sphericity and size requirements for accurate Mie calculations in the mid-visible part of the solar spectrum.

Aerosol Absorption Optical Depth (AAOD) is like AOD, but instead describes the vertical columnar integration of only the absorption coefficient, and it can be determined from AOD and SSA (Equation 1.4). For typical atmospheric aerosols, the absorption coefficient tends to account for a minority of the total extinction coefficient (Bergstrom et al., 2003). As such, AAOD tends to be only a small fraction of AOD, resulting in the former having larger relative errors. As with AOD, AAOD is also an extensive columnar property.

$$AAOD = AOD \times (1 - SSA) \;\; Equation\ 1.4$$

Extinction Ångström Exponent (EAE) describes the spectral dependence of AOD. The slope of the linear regression of logarithmic AOD over logarithmic wavelength (λ) results in a single EAE value (Equation 1.4) which can be used to represent the spectral dependence of AOD

across the entire spectrum (Russell et al., 2010). To determine unique EAE values for selected wavelengths, a quadratic regression of the same variables can instead be used. The first derivative is taken at the selected wavelengths, resulting in tangential slopes that serve as the EAE for those wavelengths. EAE is an intensive aerosol property.

$$EAE = -\frac{ln\left(\frac{AOD_{\lambda_1}}{AOD_{\lambda_2}}\right)}{ln\left(\frac{\lambda_1}{\lambda_2}\right)} \quad Equation\ 1.5$$

Absorption Ångström Exponent (AAE) is like EAE (Equation 1.6), but instead exhibits the dependence of logarithmic AAOD over logarithmic wavelength (λ). As with EAE, AAE is also an intensive aerosol property. AAE is a key tool for describing absorbing aerosol types (Russell et al., 2010). BC aerosols have an AAE near 1.0 due to their spectral uniformity of its absorption. BrC and mineral dust aerosols both exhibit spectrally dependent absorption, and thus often have AAE that depart from unity. However, BrC can still be discerned form mineral dust by observing where the most absorption is occurring, at shorter wavelengths for the former and at longer wavelengths for the latter.

$$AAE = -\frac{ln\left(\frac{AAOD_{\lambda_1}}{AAOD_{\lambda_2}}\right)}{ln\left(\frac{\lambda_1}{\lambda_2}\right)} \quad Equation\ 1.6$$

1.6 – AERONET

The determination of aerosol radiative properties necessitates the existence of instruments that can carry out high quality measurements of observed aerosols. To gain a global understanding of the spatial variability of the aerosol radiative properties, these instruments must be employed by an international research network. For ground-based observations of aerosols, that network is AERONET (AErosol RObotic NETwork). AERONET employs sun/sky photometers to measure direct solar irradiances and diffuse sky radiances, allowing for the retrieval of complex refractive index and size distribution, which are subsequently used to calculate SSA and AOD via radiative transfer theory (Holben et al., 1998; Dubovik et al., 2000).

AERONET has a global presence, with a total of about 1,100 stations across all seven continents, although the number of routinely operating AERONET stations is much lower at any given time. In addition, as is the case with nearly all large-scale geoscience projects, AERONET coverage is greatest in wealthier and more highly populated regions, leaving substantial gaps over the Arctic, Antarctica, the Sahara, the Sahel, Central Africa, and Eastern Africa. Being ground-based, AERONET has no vertical resolution, and thus relies on remote sensing via aircraft/satellites for corroboration of aerosol radiative properties in the troposphere. However, satellite retrieval of aerosol properties is limited to above-cloud aerosols, while airborne campaigns can measure both above, within, and below aerosol plumes. Thus, an airborne campaign would be ideal in a region with a persistent cloud deck.

1.7 – The Southeast Atlantic Ocean

AERONET also lacks extensive coverage in oceanic regions due to the limitations involved with being a ground-based observation network. For example, there are only three AERONET stations located in the Southeast Atlantic Ocean – São Tomé, Ascension Island, and St. Helena. And of these three, the São Tomé station was in operation for only one year (06/2017-10/2018).

Southern Africa accounts for almost a third of global BB aerosol emissions due to savannah/forest burning and residential outdoor cooking practices, amongst other sources (van der Werf et al., 2010). The aerosol smoke plumes are then transported by easterly jets for up to ten days before reaching the SE Atlantic (Adebiyi & Zuidema, 2016). The BB aerosols then interact with a semipermanent subtropical stratocumulus cloud deck in complex processes that are associated with a high degree of uncertainty (Sakaeda et al., 2011). This uncertainty is reflected by large GCM residuals persistent in the region (Mallet et al., 2021).

1.8 – ORACLES

The ORACLES (ObseRvations of Aerosols above CLouds and their intEractionS) 2016-2018 suborbital airborne campaigns were conducted by NASA and collaborators to investigate BB aerosol transport, aerosol-cloud interactions, and aerosol-radiation processes over the SE Atlantic (Redemann et al., 2021). In 2016, ORACLES was based out of Walvis Bay, Namibia; while in 2017-2018, it was based out of São Tomé (Figure 1.3). A NASA Airborne Science Program P-3 Orion research aircraft (N426NA) was deployed for all three campaigns, with a high-altitude ER-2 aircraft (N809NA) also deployed in 2016 for remote sensing and multi-aircraft comparison of aerosol/cloud property retrievals (Pistone et al., 2019). The P-3 housed 15 instruments, including 4STAR (see Materials and Methods for more information). Each of the three campaigns lasted for about a month (September, August, and October, respectively) so that conclusions about the subseasonal variability of BB aerosols could be drawn from the cumulative dataset (Redemann et al., 2021).

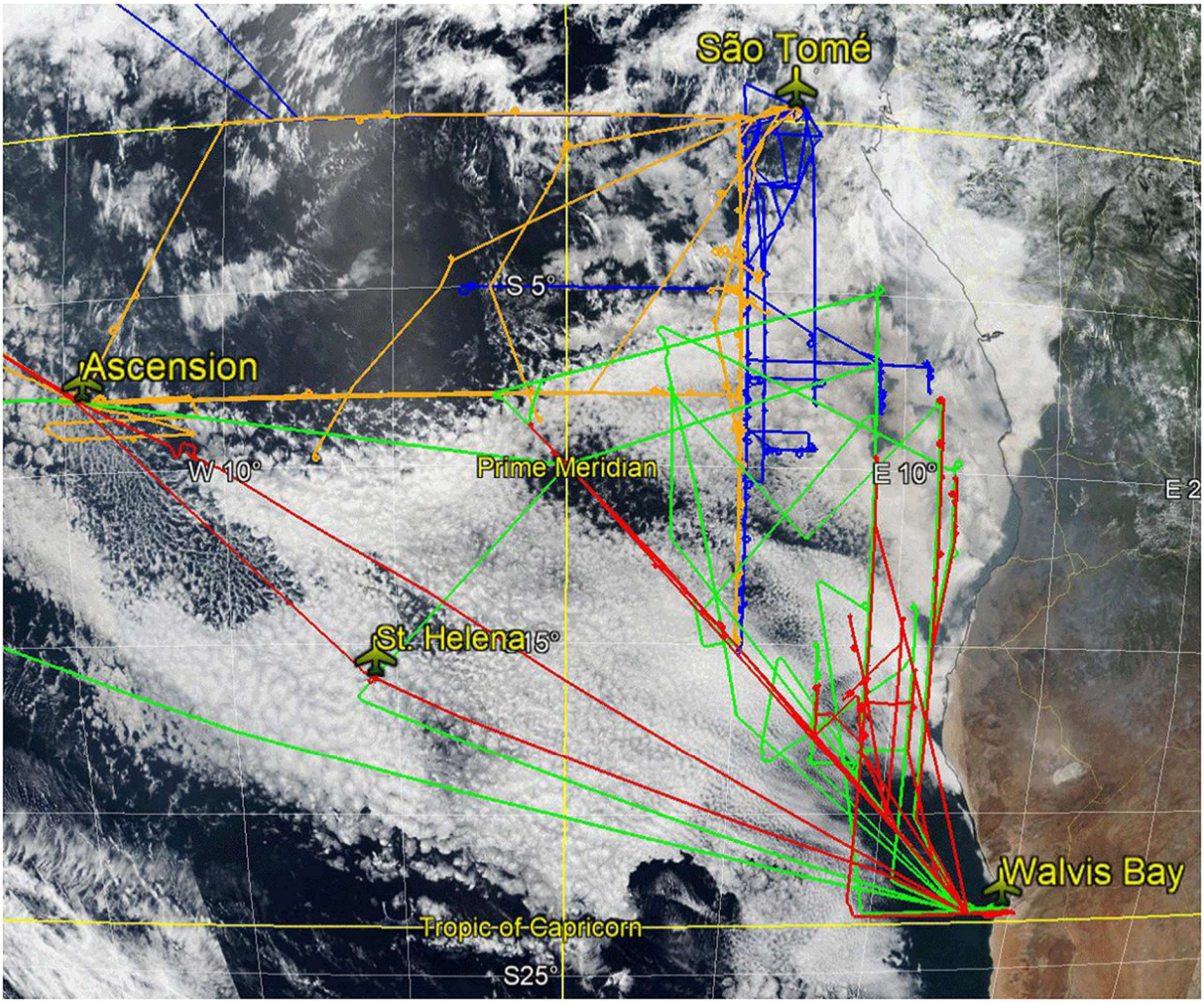

Figure 1.3 – The ER-2 2016 (green), P-3 2016 (red), P-3 2017 (orange), and P-3 2018 (blue) flight tracks. The campaign headquarters at Walvis Bay, Namibia, and São Tomé are labelled, as are the refueling stations at Ascension Island and St. Helena. The stratocumulus cloud deck is visible over the SE Atlantic, in white. Adapted from Redemann et al., 2021.

1.9 – The BB Emission Season

BB aerosol emissions in Southern Africa are greatest from August to October (Zuidema et al., 2016), which aligns, by design, with the temporal extent of the ORACLES campaigns. Since the emissions are consistently strongest during that time, this period will be denoted as the BB emission season. Hence, changes in aerosol radiative properties within that period will be referred to as the subseasonal variability of that property.

Observations from AERONET stations help to uncover the subseasonal variability of SSA and AOD (Figure 1.4) over Southern Africa from 1995 to 2013 (Redemann et al., 2021). SSA displays an upward curving trend, decreasing from a mean of about 0.875 in July to about 0.85 in August, but then increasing to about 0.92 by November. This subseasonal variation in SSA is large enough (about 0.7) that, in concert with surface albedo, it can significantly impact aerosol-induced radiative flux (Russell et al., 2002). AOD, conversely, displays a downward curving trend, increasing from a mean of about 0.2 in July to about 0.6 in September, but then decreasing back to 0.25 by November. These subseasonal variations in AOD are most likely a function of changes in aerosol loading. Since Southern Africa is the source region for the BB aerosols found over the SE Atlantic, we would expect to see similar subseasonal variability of BB aerosols, albeit delayed by transport for up to ten days (Adebiyi & Zuidema, 2016).

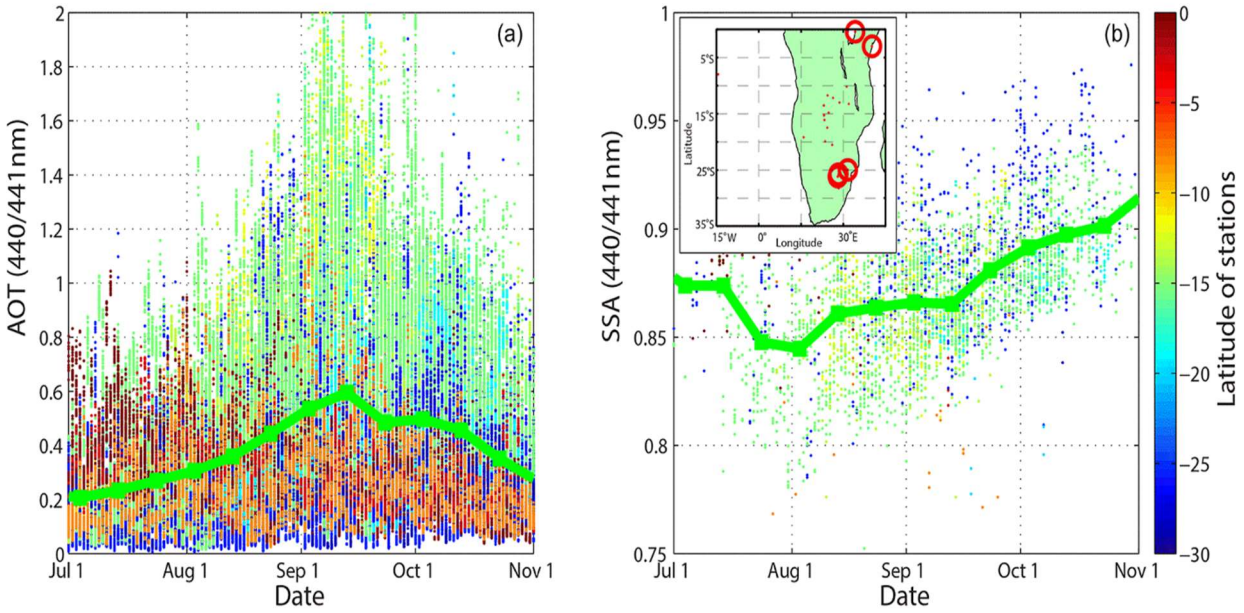

Figure 1.4 – Subseasonal variability of AOD (left) and SSA (right) at 440 nm from AERONET stations in Southern Africa, during 1995-2013. In the inset map, small red dots denote historical AERONET stations, while larger red circles denote AERONET stations still active during 2011-2013. Adapted from Redemann et al., 2021.

1.10 – Thesis Statement

The primary goal of this thesis is to investigate the subseasonal variability of aerosol radiative properties over the SE Atlantic. The subseasonal variability of each radiative property will reveal additional information regarding BB aerosol-cloud-radiation interactions in the SE Atlantic stratocumulus cloud deck: SSA will hint at changes in scattering/absorption, AOD will reveal changes in aerosol loading, AAOD will confirm the changes in scattering/absorption suggested by SSA, and AAE will unveil changes in aerosol type. If the subseasonal variability of SSA is greater than 0.5, as is the case for the Southern Africa AERONET data (Redemann et al., 2021), then there will be significant implications for the calculation of aerosol-induced radiative flux over the SE Atlantic (Russell et al., 2002). The subseasonal variability of AAE will speak to whether the changes in scattering/absorption are attributable to the mix of aerosol types (Bond et al., 2013) or the evolution of BB aerosol composition (Eck et al., 2013).

The secondary goal of this thesis is to compare the subseasonal variability of aerosol radiative properties from ORACLES against AERONET. This will allow for comparing the two datasets in three ways: spatially, temporally, and methodologically. Spatially, differences in aerosol radiative properties between the upwind source region of Southern Africa and the downwind study region of the SE Atlantic can be observed, and the influence of BB aerosol transport noted. Temporally, the shorter ORACLES 2016-2018 campaigns can be placed in the context of the extended AERONET 1995-2013 record (Redemann et al., 2021) to exhibit the continuation of subseasonal trends. And methodologically, contrasting the two datasets will speak to the effectiveness of the 4STAR instrument employed in the ORACLES campaigns to serve as an airborne version of a traditional ground-based AERONET station.

Chapter 2 – Materials and Methods

2.1 – 4STAR

4STAR (Spectrometer for Sky-Scanning, Sun-Tracking Atmospheric Research) is the hyperspectral sun-sky spectrophotometer (Figure 2.1) employed in all three ORACLES campaigns for measuring above-aircraft, below-plume columnar properties (Dunagan et al., 2013; Pistone et al., 2019). 4STAR has three operating modes – sky scanning, sun tracking, and zenith viewing.

For zenith viewing mode, 4STAR is oriented directly upwards to measure cloud radiances for the retrieval of cloud droplet size and Cloud Optical Depth (COD). During sun tracking, 4STAR remains focused on the sun so that it can measure direct solar irradiances transmitted through aerosols, cirrus clouds, and other gases. This is used to infer AOD, EAE, and cirrus cloud properties.

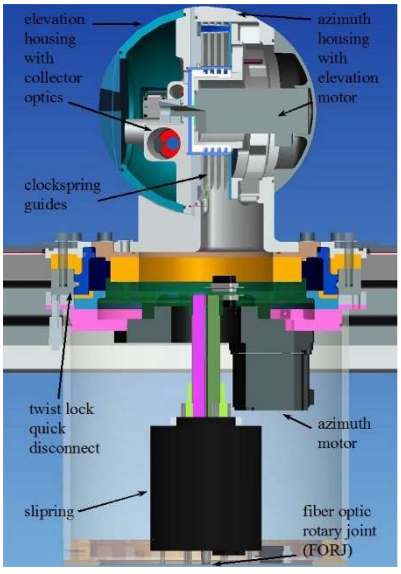

Figure 2.1 – Diagram of the 4STAR instrument. Adapted from Dunagan et al., 2013.

The final operating mode is sky scanning. While sky scanning, 4STAR uses either almucantar (ALM) or principal plane (PPL) scanning methods to measure diffuse sky radiances scattered by atmospheric aerosols. For PPL scanning, 4STAR scans in a path directly perpendicular to the sun. PPL scanning enjoys widespread scientific use due to its larger range of SA and its improved accuracy near solar noon. During ALM scanning, 4STAR scans in clockwise (CW) and counterclockwise (CCW) legs on both sides of the sun. A sky symmetry test can then be performed on the two ALM legs. ALM scans that pass this sky symmetry test can achieve higher levels of QA/QC than PPL scans (Pistone et al., 2019), but ALM scans that fail the sky symmetry test due to non-uniformity may be unable to determine an ALM average for the two legs. Thus, 4STAR's use of both scanning methods allows for ALM scans to establish sky homogeneity, which can then also be assumed for PPL scans that follow in quick succession. Both methods measure sky radiances, which allow for the retrieval of aerosol size distribution and complex refractive index, which are then used to calculate SSA.

2.2 – AERONET Adapted Retrieval Code

The code utilized in this thesis work is a version of AERONET code (Holben et al., 1998; Dubovik et al., 2000) that was adapted by Dr. Connor Flynn for the retrieval of 4STAR aerosol properties via MATLAB (MATrix LABoratory) computational software. The primary input for batch sky scan processing is daily resolution star.mat compilation files that contain all the data and metadata recorded during that day's research flights. The secondary input is daily resolution SSFR.ict files from P-3 flights containing spectral shortwave irradiances that are used to calculate instantaneous flight-level albedo concurrent with 4STAR measurements. The SSFR (Solar Spectral Flux Radiometer) measures nadir upwelling irradiances and zenith downwelling irradiances (Pistone et al., 2019; Cochrane et al., 2022) during the plane's square spiral descent through the plume (Figure 2.2). The SSFR.ict files were downloaded from the NASA ESPO (Earth Science Project Office) ORACLES data archive.

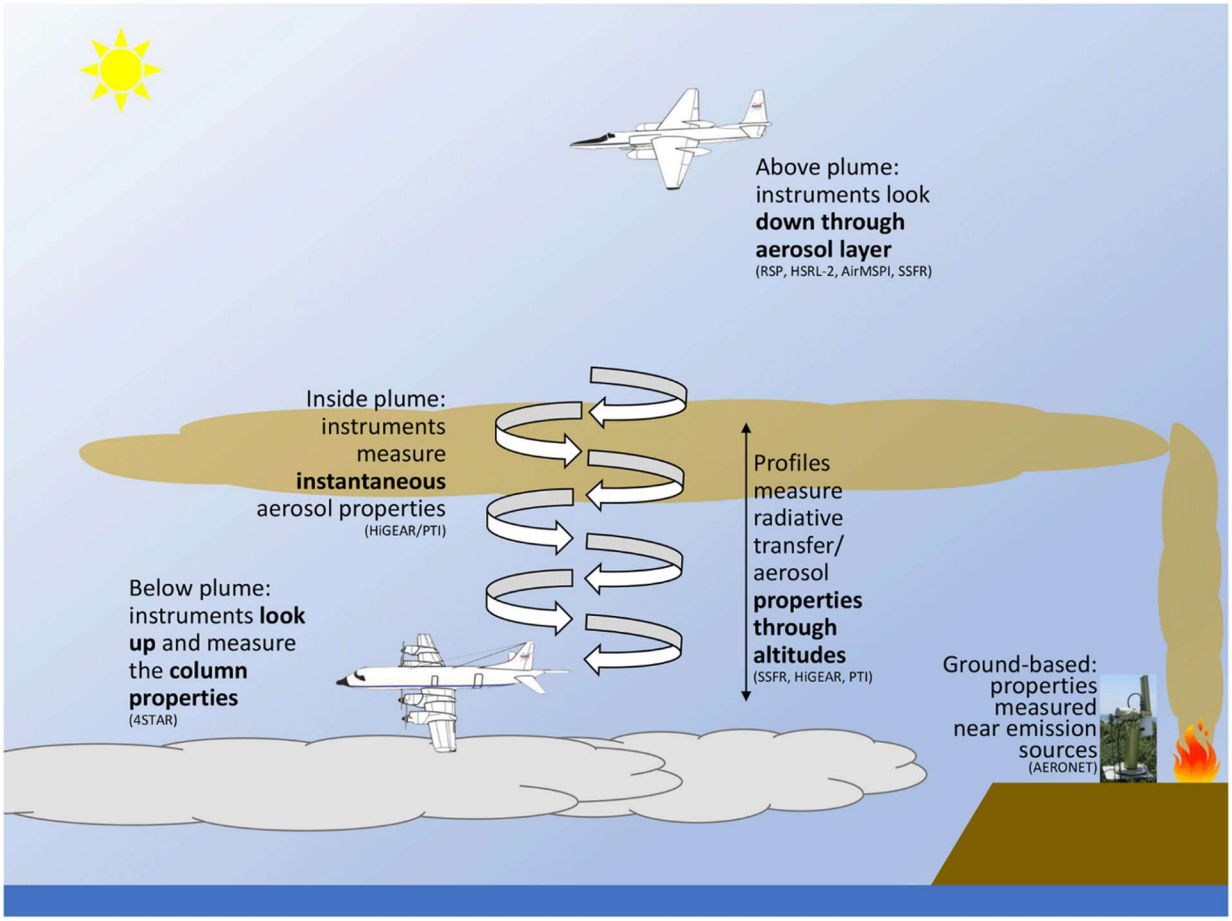

Figure 2.2 – ORACLES flight diagram. The higher aircraft is the ER-2 (2016), which remains at high altitudes throughout its flights. The lower aircraft is the P-3 (2016-2018), which flies above, within, and below the aerosol plume. The ground-based station represents the AERONET network in Southern Africa. Instruments of note include 4STAR and SSFR, which operate during the below plume and square spiral descent phases, respectively.

Adapted from Pistone et al., 2019.

This batch processing produces skyscan.input and skyscan.mat files containing all the data and metadata for each individual sky scan. This results in ppl.input files for PPL scans, almA.input files for the CCW leg of ALM scans, and almB.input files for the CW leg of ALM scans. If the CCW and CW legs agree, then an avg.input file is created for the entire ALM scan. Figures generated by this code include flight telemetry (Figure 2.3), SSFR irradiances and albedo (Figure 2.4), sky radiances as a function of SA (Figure 2.5), AOD/AGOD (Absorbing Gas Optical Depth) over wavelength (Figure 2.6), CCW/CW adjustments (ALM only), and SA/elevation angle adjustments (PPL only).

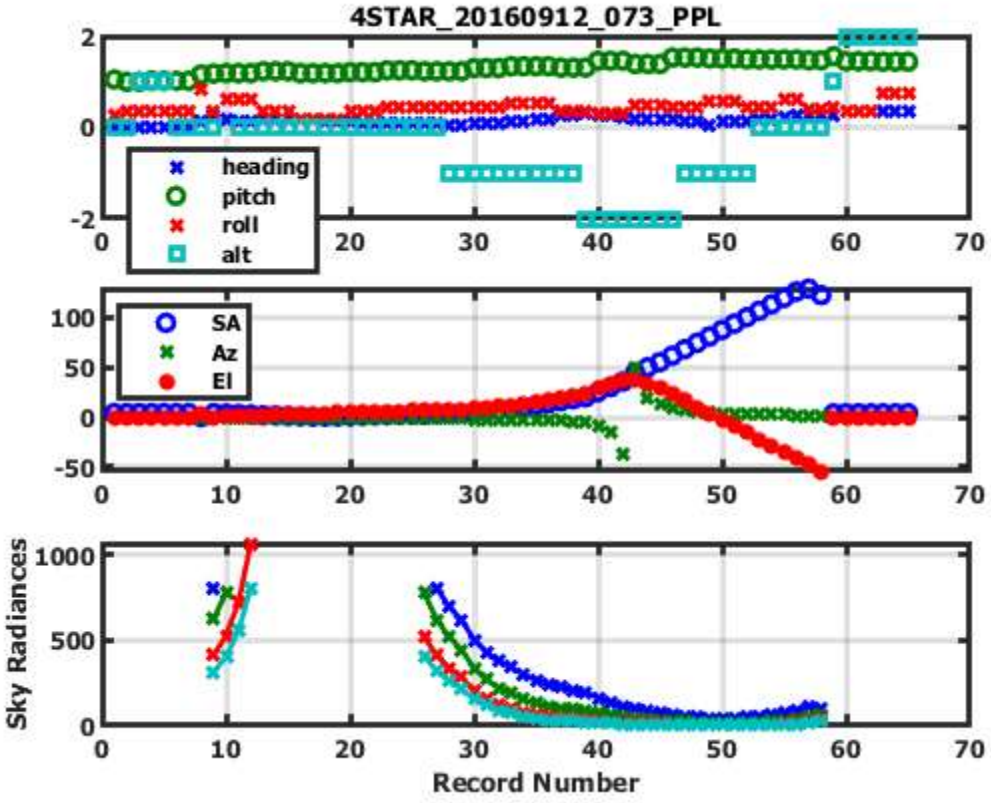

Figure 2.3 – Flight telemetry from the 2016/09/12 #73 PPL sky scan. This sky scan was among those included by Pistone et al. (2019) in a case study comparison of 4STAR-retrieved SSA, AOD, and AAOD against those from the in situ PSAP (Particle Soot Absorption Photometer) and nephelometer, as well as the RSP (Research Scanning Polarimeter). The top panel is of flight metadata, including altitude, heading, pitch, and roll. The middle panel is of optical angles recorded by 4STAR, including SA, azimuth angle, and elevation angle. The bottom panel is of when sky radiance measurements occurred.

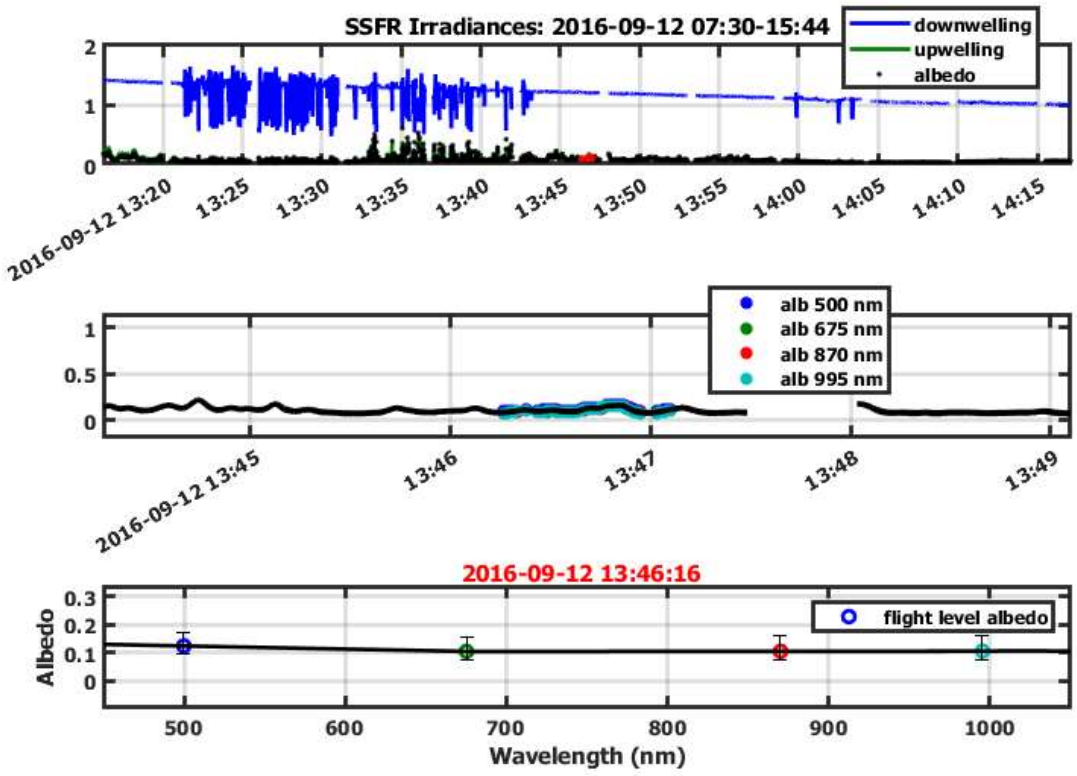

Figure 2.4 – SSFR irradiances and albedo from the 2016/09/12 #73 PPL sky scan. In the top panel, there are notable fluxes in zenith downwelling irradiances between 13:20 and 13:45 UTC. The middle panel is of flight-level albedo, with values retrieved between 13:46 and 13:48 UTC. The bottom panel is of SSFR-retrieved flight-level albedo over wavelength.

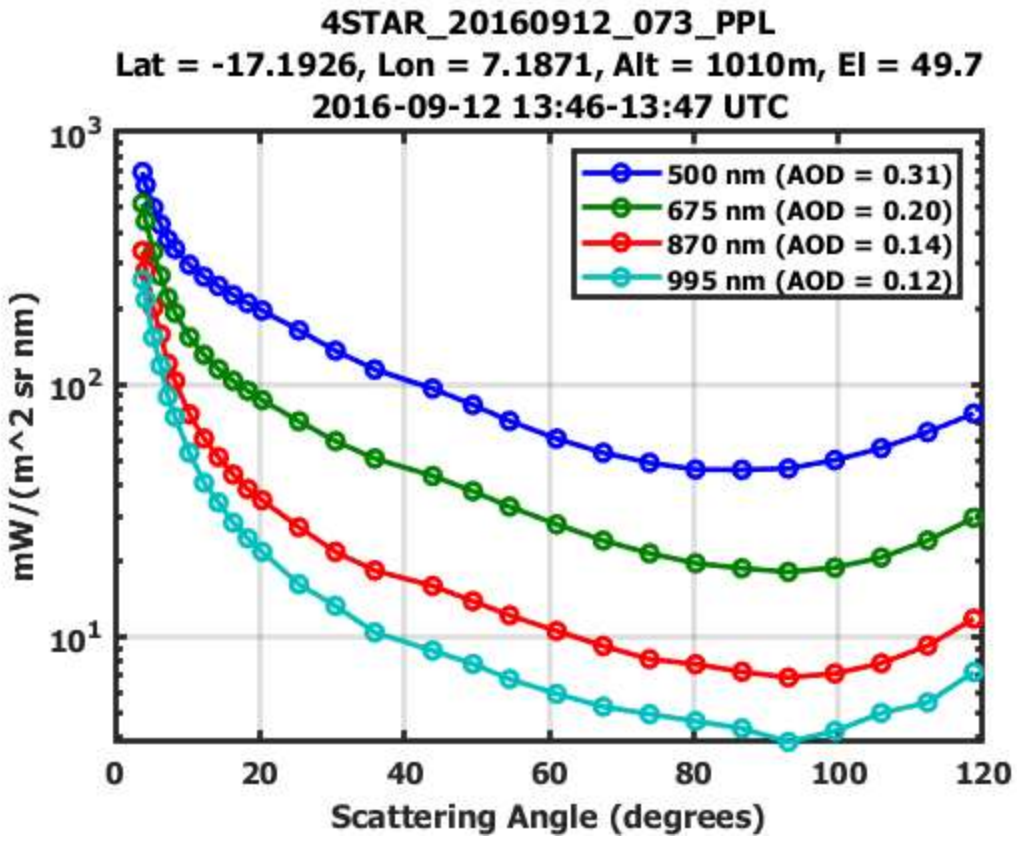

Figure 2.5 – Sky radiances as a function of SA from the 2016/09/12 #73 PPL sky scan.

The unbroken sky radiances from 3.5° to 120° SA speak to the high quality of this sky scan.

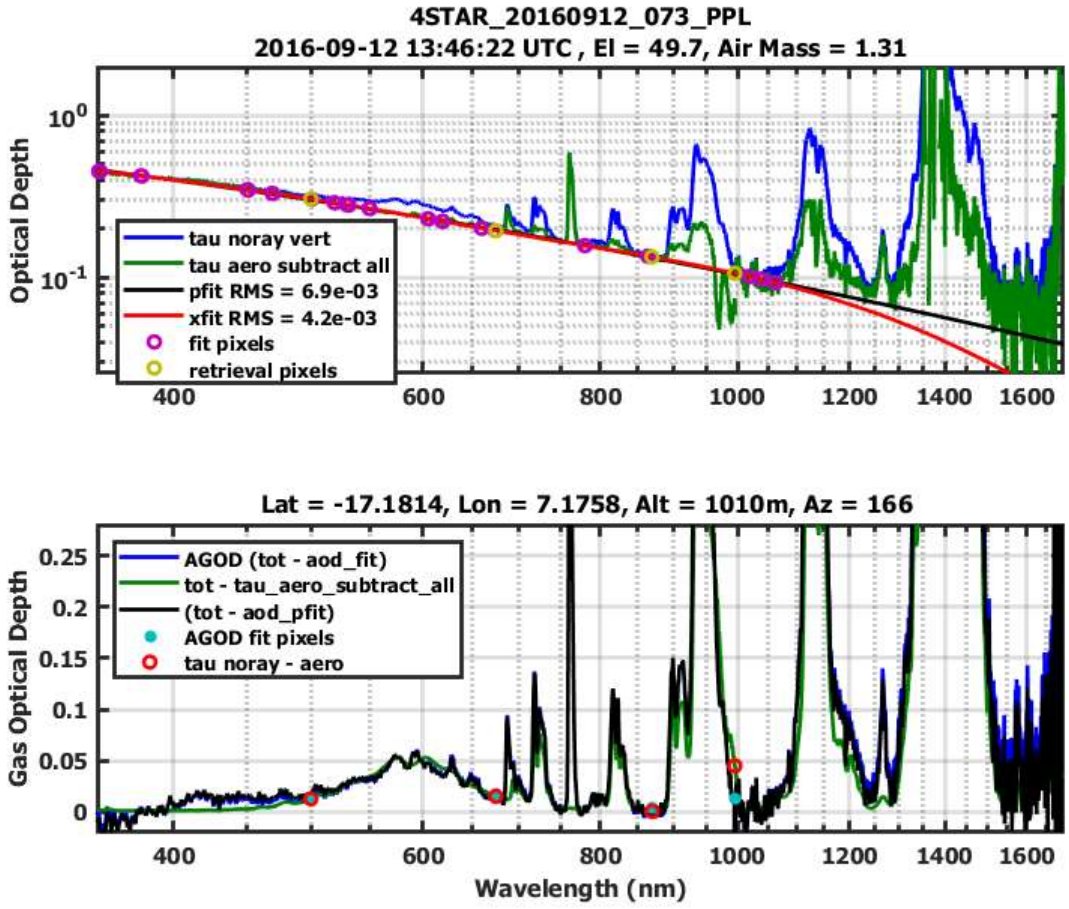

Figure 2.6 – Spectral AOD and AGOD from the 2016/09/12 #73 PPL sky scan. In the top panel, the black line is the polynomial fit employed by the AERONET-adapted code for 4STAR retrievals, which trends along the bottom of the calculated AOD, ignoring the absorbing gas bands in the longer wavelengths. In the bottom panel, the difference between calculated AOD and the AGOD fit at 995 nm makes the influence of the absorbing gas bands even more apparent, with the impact of the instrument artifact also visible between 400 and 450 nm.

The next step is batch retrieval. For this thesis work, only sky scans that generated ppl.input or avg.input were supplied to the retrieval code, as to exclude non-uniform ALM scans. The retrieval code uses aerosol size distribution and sky radiances (Figure 2.7), as well as complex refractive index (Figure 2.8), as inputs for radiative transfer theory calculations, resulting in aerosol radiative properties, including SSA, AOD, AAOD, EAE, and AAE (Figure 2.8). These retrieved values are saved as both retrieval.output and retrieval.mat files for each individual sky scan.

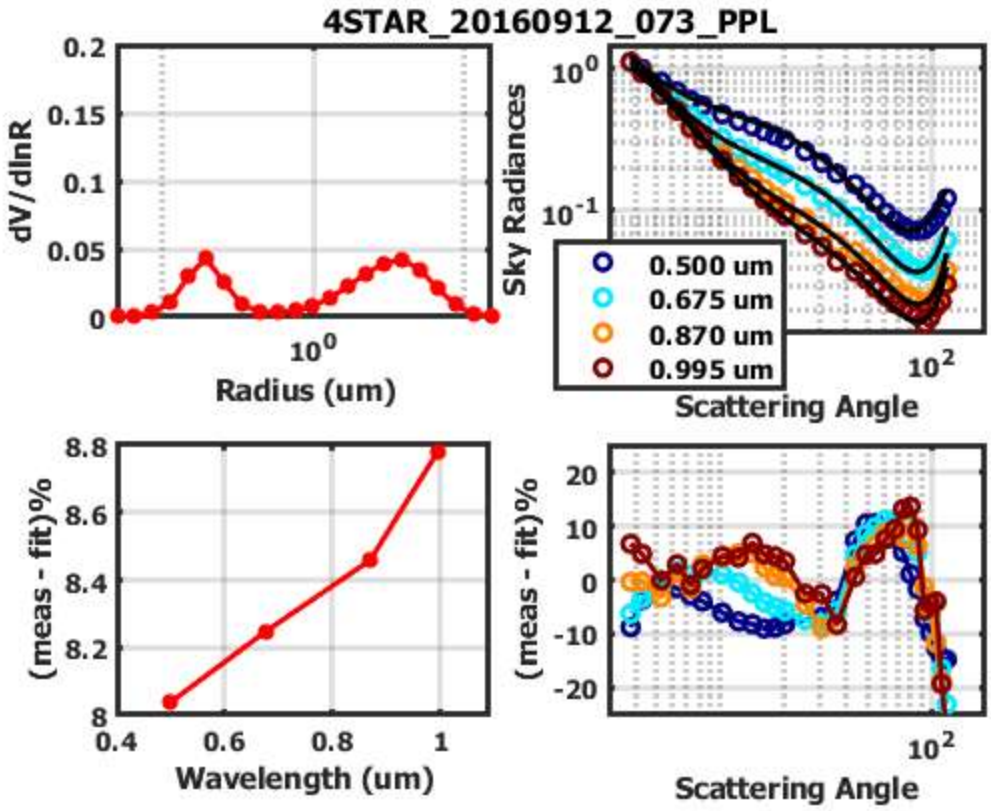

Figure 2.7 – Volumetric size distribution and sky radiances as a function of SA (as well as their deviations from fit) from the 2016/09/12 #73 PPL retrieval. The bimodal size distribution in the upper-left panel displays fine and course modes as distinct relative maxima. The upper-right panel compares the sky radiances to their fits, displaying general agreement between the two at all wavelengths. This is echoed by the lower-right panel, which shows that the error remains within ±10% and only regularly exceeds that threshold above an SA of 50°. The lower-left panel is the integral of the sky radiance error, and it shows that the size distribution difference from fit remains under 10% throughout the spectrum, with the error increasing with wavelength.

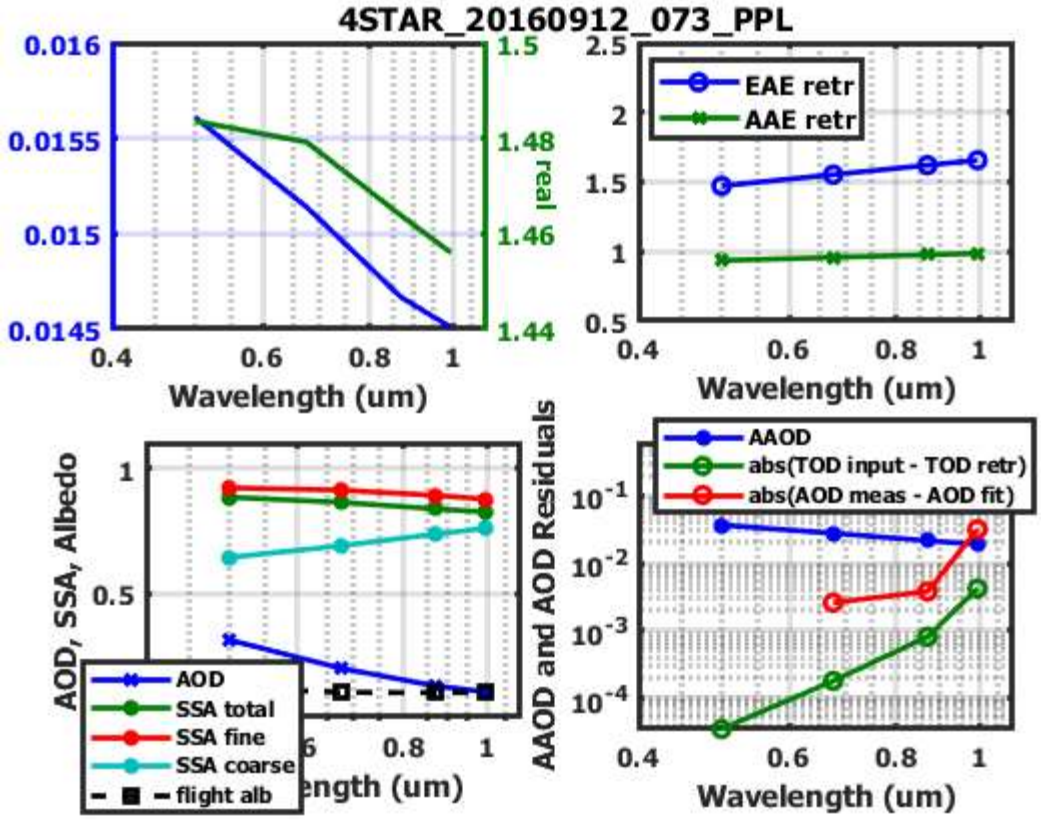

Figure 2.8 – Complex refractive index, SSA, AOD, AAOD, EAE, and AAE from the 2016/09/12 #73 PPL retrieval. The upper-left panel is of real (green) and imaginary (blue) refractive index, with both decreasing with increasing wavelength. The lower-left panel is of 4STAR-retrieved AOD and SSA (including total, fine mode, and coarse mode), as well as SSFR-retrieved flight-level albedo. The lower-right panel is of 4STAR-retrieved AAOD and differences between expectations/reality for AOD and TOD (Total Optical Depth). The upper-right panel is of 4STAR-retrieved EAE and AAE.

2.3 – Wavelength Selection

Special consideration was given to the selection of the wavelength set that would be used during sky scan processing and retrieval. In the current AERONET-adapted code, the retrieved values are dependent upon the wavelengths of the input sky radiances, such that differing wavelength selections will yield varying results. This is especially true of the shortest and longest wavelengths used (particularly the shortest), as they act to "bound" the inputs to the polynomial fitting routine.

Although a five-wavelength set of 400, 500, 675, 870, and 995 nm was appropriate for the Pistone et al. (2019) analysis of ORACLES 2016 sky scans, this wavelength set could not be utilized for an analysis of the entire ORACLES 2016-2018 campaigns. This is because an instrument artifact impacting AOD values near 425 nm was present during the 2017 and 2018 campaigns, such that the accuracy of 400 nm retrievals during those years would be greatly reduced. Another reason is that the 4STAR instrument was found to be affected by stray light scattering below 400 nm during 2018 Langley calibrations at Mauna Loa, Hawaii. This means that even if the instrument artifact was avoided by instead selecting an ultraviolet wavelength (such as 360 or 380 nm), then the measurements would still be affected by stray light scattering, which would have to undergo arduous levels of processing to correct for. As such, we instead settled upon a four-wavelength set of 500, 675, 870, and 995 nm as to avoid both the instrument artifact and stray light scattering issues, although resolving these problems in the future will extend retrievals into the ultraviolet range and enhance 4STAR capabilities for the classification of aerosol types (Russell et al., 2010).

To establish whether our four-wavelength set yielded statistically similar results to the Pistone et al. (2019) five-wavelength set, the difference between the two sets was taken for both

SSA and AAOD, at the four overlapping wavelengths (Figure 2.9). The median difference in SSA and AAOD was statistically zero for 675-995 nm, while the 500 nm results showed slight biases, with a negative SSA median bias of -0.004 and a corresponding positive AAOD median bias of 0.002, both of which are essentially insignificant within quoted accuracies. In addition, the interquartile ranges of the differences remain small for both SSA (under 0.01) and AAOD (under 0.004).

A bisector least square regression was also taken between the two wavelength sets for both SSA and AAOD, at each overlapping wavelength. The bisector least squares regression differs from ordinary least squares regression by treating neither variable as truth, which minimizes perpendicular fit error instead of vertical fit error. The regressions showed that both SSA (Figure 2.10) and AAOD (Figure 2.11) had tight agreement between the two wavelength sets for 675-995 nm, with only a high SSA cluster (mostly above 0.8) and high AAOD outliers (mostly above 0.1) causing any noticeable deviation from unity at 500 nm.

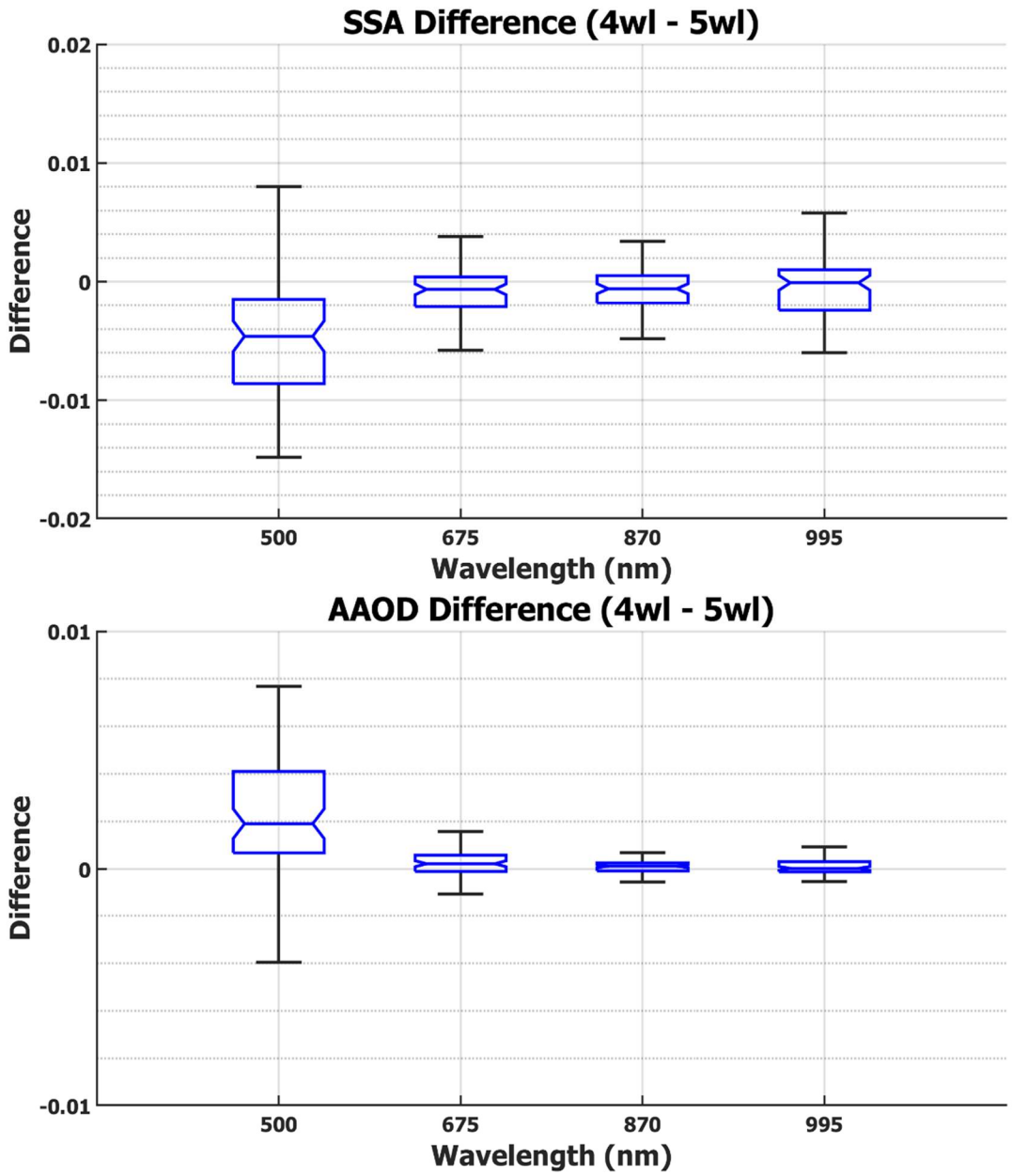

Figure 2.9 – Boxplots of SSA (top) and AAOD (bottom) differences between the four-wavelength and five-wavelength sets.

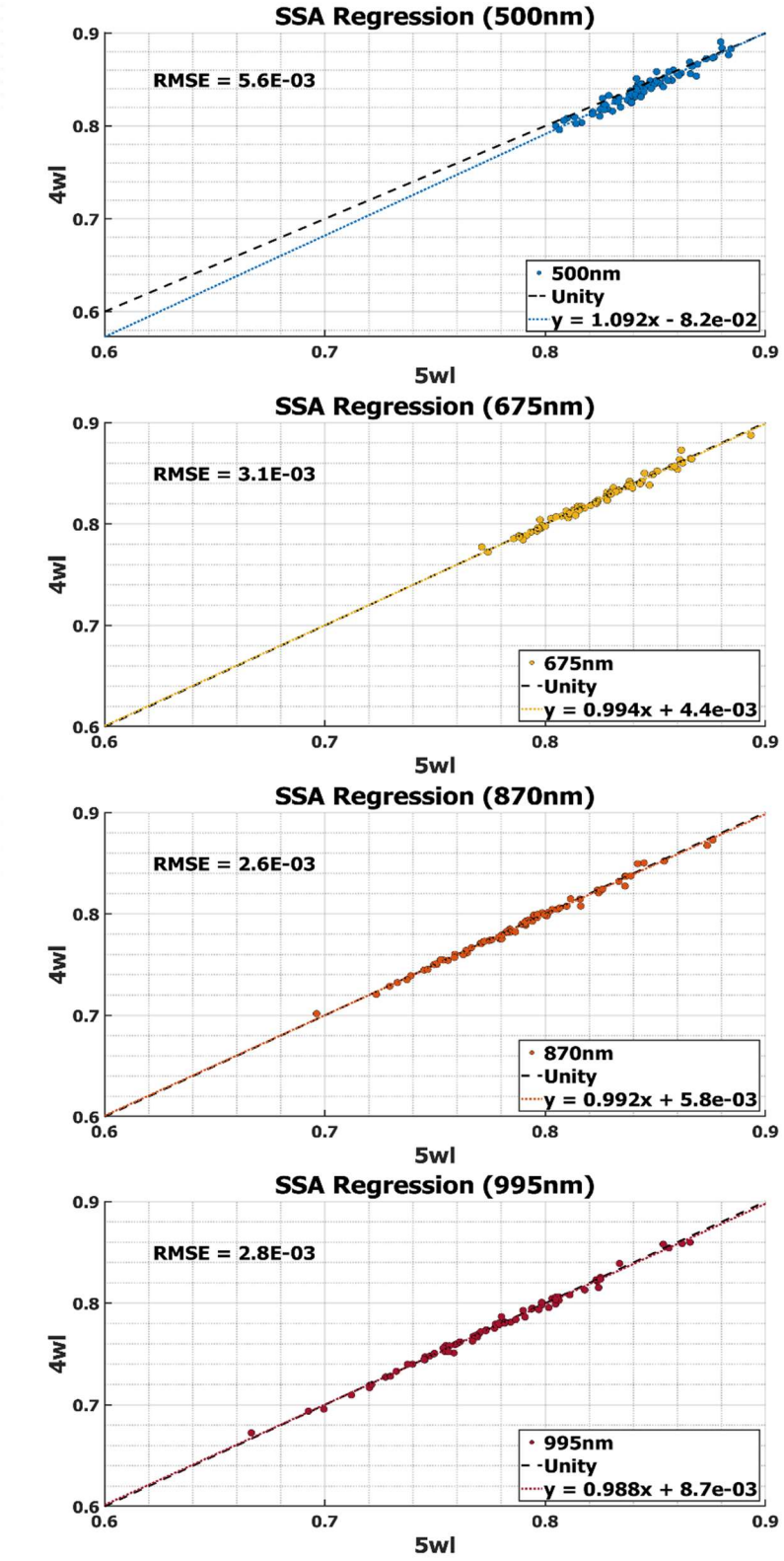

Figure 2.10 – Bisector least squares regressions of SSA between the four-wavelength and five-wavelength sets at 500 (first), 675 (second), 870 (third), and 995 nm (fourth).

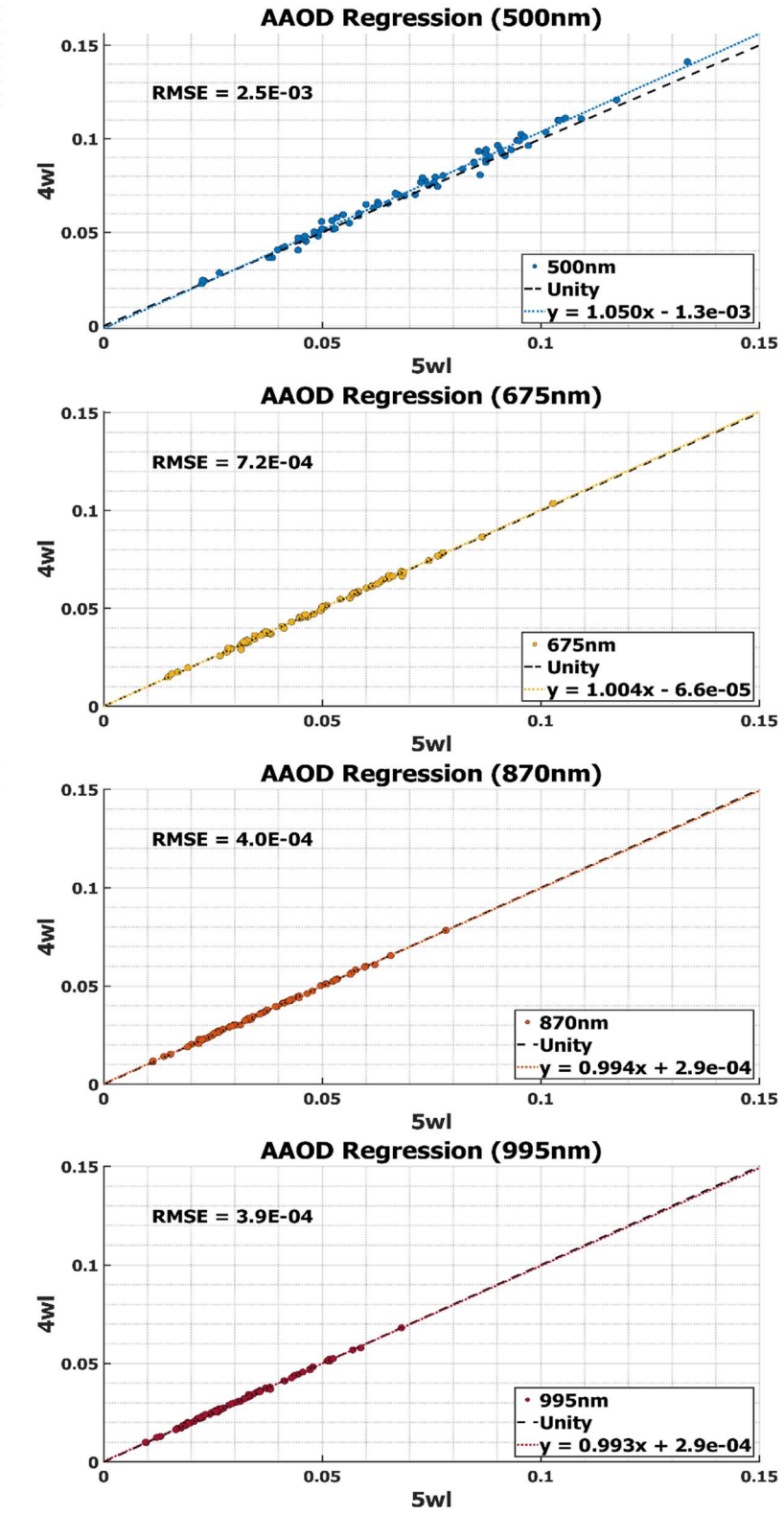

Figure 2.11 – Bisector least squares regressions of AAOD between the four-wavelength and five-wavelength sets at 500 (first), 675 (second), 870 (third), and 995 nm (fourth).

2.4 – Quality Assurance/Quality Control

To improve the accuracy of the 4STAR-retrieved aerosol radiative properties utilized in the subseasonal analysis, we excluded sky scans that failed to meet defined QA/QC criteria. These criteria were adapted from Pistone et al. (2019), and are as follows:

- calculated polynomial fit AOD > 0.2 at 400 nm
- flight altitude < 3 km
- flight altitude variation < 50 m
- sky error (coarse SSA) < 10%
- SA span 3.5 – 50°, with at least 6 unique SA values for the critical range of 3.5 – 30°

These requirements are not as strict as AERONET version 2.0 QA criteria which requires AOD at 440 nm > 0.4. Such conditions are rarely present aloft, so the inclusion of AOD in the 0.2 – 0.4 range allows for the examination of radiative properties during typical lower aerosol loadings. The inclusion of PPL scans is also appropriate given that sky homogeneity is established by preceding ALM scans. The flight altitude requirement excludes any sky scans that are well above the stratocumulus cloud deck.

This QA/QC procedure was applied to sky scans from all three years of ORACLES campaigns. This resulted in QA/QC being met for 82 of the 173 (47%) total sky scans from 2016 (Table 2.1), 143 of the 338 (42%) total sky scans from 2017 (Table 2.2), and 83 of the 229 (36%) total sky scans from 2018 (Table 2.3). For 2016, 73 of the 82 sky scans were the same ones utilized in Pistone et al. (2019), an overlap of 87%.

Table 2.1 – The 82 sky scans utilized from the ORACLES 2016 campaign.

Date	Scan No.	Scanning Method	Time (UTC)	Latitude (°)	Longitude (°)	Altitude (m)	Elevation Angle (°)	Flight Level Albedo	AOD (500nm)
20160831	13	ALM	9:21	-19.78	9.70	2374	54.44	0.66	0.18
20160831	14	PPL	9:22	-19.72	9.64	2374	101.52	0.57	0.20
20160831	117	ALM	13:31	-17.10	6.99	1174	55.46	0.70	0.60
20160831	118	PPL	13:33	-17.05	6.93	1168	86.12	0.72	0.61
20160831	124	PPL	13:37	-17.07	6.87	1169	84.47	0.72	0.61
20160831	127	ALM	13:38	-17.13	6.94	1164	55.67	0.69	0.61
20160831	133	ALM	14:08	-18.27	8.10	1036	47.55	0.72	0.45
20160831	134	PPL	14:10	-18.32	8.15	1036	94.71	0.69	0.43
20160902	18	ALM	8:26	-18.75	10.00	890	43.97	0.61	0.46
20160902	19	PPL	8:28	-18.66	10.00	895	92.55	0.64	0.46
20160902	22	ALM	8:29	-18.51	10.00	892	45.01	0.62	0.42
20160902	23	PPL	8:31	-18.42	10.00	892	92.64	0.56	0.38
20160902	26	ALM	8:37	-17.94	10.00	946	46.83	0.70	0.32
20160902	27	PPL	8:38	-17.85	10.00	945	95.79	0.63	0.32
20160902	31	PPL	9:14	-15.02	10.00	1551	103.10	0.69	0.39
20160902	34	ALM	9:18	-14.73	10.00	1090	56.34	0.76	0.48
20160902	35	PPL	9:19	-14.65	10.00	1090	104.31	0.81	0.49
20160902	43	PPL	9:32	-14.47	10.01	1354	113.95	0.55	0.50
20160902	46	ALM	9:33	-14.59	10.01	1351	61.70	0.62	0.50
20160902	53	PPL	10:32	-16.22	8.59	956	110.06	0.53	0.39
20160902	61	PPL	10:59	-15.68	9.13	977	111.75	0.62	0.43
20160902	72	ALM	12:29	-14.93	8.59	1043	66.44	0.66	0.49
20160902	73	PPL	12:30	-14.86	8.57	1043	108.68	0.63	0.51
20160902	82	PPL	12:32	-14.76	8.54	1045	107.84	0.62	0.52
20160902	93	PPL	14:49	-22.98	14.16	1283	79.77	0.12	0.38
20160904	16	PPL	9:04	-19.14	9.02	811	98.34	0.42	0.46
20160904	19	ALM	9:06	-19.06	8.93	798	51.43	0.51	0.47
20160904	46	PPL	10:39	-14.07	3.88	1050	108.84	0.45	0.57
20160904	49	ALM	10:40	-14.00	3.81	1100	67.87	0.62	0.54
20160906	32	ALM	9:33	-16.16	9.00	873	58.95	0.63	0.31
20160906	33	PPL	9:35	-16.07	9.00	895	102.91	0.75	0.31
20160906	39	ALM	10:05	-13.78	9.00	921	66.90	0.49	0.42
20160906	40	PPL	10:06	-13.69	9.00	962	111.11	0.43	0.41
20160906	55	PPL	10:58	-9.78	9.00	1033	117.24	0.63	0.57
20160906	69	PPL	11:50	-12.99	9.52	2589	115.25	0.46	0.22
20160906	72	ALM	12:25	-15.72	10.48	2260	67.76	0.53	0.28
20160906	73	PPL	12:26	-15.81	10.51	2262	111.18	0.56	0.26
20160906	79	ALM	13:08	-18.49	11.49	656	57.04	0.45	0.45
20160906	80	PPL	13:09	-18.56	11.52	653	102.39	0.47	0.45

Date	Scan No.	Scanning Method	Time (UTC)	Latitude (°)	Longitude (°)	Altitude (m)	Elevation Angle (°)	Flight Level Albedo	AOD (500nm)
20160908	11	PPL	11:13	-10.93	0.94	1206	117.66	0.09	0.29
20160908	85	ALM	13:09	-17.21	7.20	1126	61.48	0.45	0.27
20160910	50	PPL	11:04	-14.38	4.50	1317	113.91	0.57	0.34
20160910	61	PPL	12:18	-14.23	4.21	1318	113.49	0.46	0.37
20160912	25	PPL	12:14	-12.33	2.37	1231	117.83	0.53	0.40
20160912	44	ALM	13:08	-15.35	5.35	1928	65.39	0.43	0.34
20160912	45	PPL	13:09	-15.41	5.41	1927	109.21	0.57	0.33
20160912	48	PPL	13:10	-15.47	5.47	1929	108.94	0.36	0.34
20160912	72	ALM	13:45	-17.15	7.15	1017	56.89	0.13	0.32
20160912	73	PPL	13:46	-17.20	7.19	1009	99.61	0.14	0.31
20160912	76	ALM	14:06	-18.03	8.03	80	50.40	0.06	0.37
20160912	77	PPL	14:08	-18.07	8.07	82	98.43	0.05	0.37
20160914	4	ALM	9:18	-19.31	9.78	778	57.46	0.43	0.31
20160914	5	PPL	9:19	-19.23	9.73	777	103.11	0.50	0.31
20160914	11	ALM	10:30	-17.79	9.00	815	68.62	0.50	0.36
20160914	14	ALM	10:37	-17.38	9.00	835	69.34	0.45	0.37
20160914	17	PPL	10:39	-17.26	9.00	848	111.26	0.37	0.38
20160918	10	PPL	9:50	-10.80	11.50	1216	114.00	0.68	0.40
20160920	27	PPL	9:25	-16.54	10.50	625	107.02	0.62	0.57
20160920	30	ALM	9:27	-16.42	10.50	628	62.02	0.71	0.55
20160920	33	PPL	9:28	-16.33	10.50	627	105.98	0.69	0.57
20160920	36	ALM	9:31	-16.19	10.50	623	63.21	0.67	0.59
20160920	39	PPL	9:33	-16.07	10.50	626	107.76	0.71	0.68
20160920	42	ALM	9:34	-15.99	10.50	629	63.86	0.74	0.64
20160920	62	PPL	11:01	-16.19	9.00	644	115.40	0.46	0.78
20160920	66	PPL	11:03	-16.03	9.00	668	114.26	0.58	0.78
20160920	75	PPL	11:08	-15.75	9.00	725	116.17	0.63	0.94
20160920	170	PPL	13:14	-17.60	9.00	767	99.20	0.44	0.64
20160920	179	PPL	13:17	-17.72	9.00	786	104.58	0.40	0.63
20160920	182	PPL	13:18	-17.83	9.00	787	106.72	0.42	0.64
20160920	185	ALM	13:23	-18.09	9.07	791	60.91	0.45	0.60
20160924	31	PPL	9:42	-10.34	11.00	2084	114.10	0.28	0.59
20160924	35	PPL	9:48	-9.91	11.00	1424	110.22	0.31	0.62
20160924	89	PPL	11:55	-10.04	11.00	2102	119.56	0.09	0.60
20160925	34	PPL	11:45	-10.61	0.61	1376	122.74	0.52	0.53
20160925	59	ALM	13:54	-14.41	4.41	1113	58.74	0.66	0.36
20160925	62	ALM	13:58	-14.62	4.62	1213	57.10	0.63	0.34
20160925	63	PPL	13:59	-14.68	4.68	1210	102.15	0.64	0.34
20160925	66	ALM	14:03	-14.90	4.89	1272	56.80	0.54	0.33
20160925	67	PPL	14:05	-14.94	4.94	1272	102.12	0.54	0.33

Date	Scan No.	Scanning Method	Time (UTC)	Latitude (°)	Longitude (°)	Altitude (m)	Elevation Angle (°)	Flight Level Albedo	AOD (500nm)
20160925	80	ALM	15:18	-19.48	9.47	1229	32.55	0.62	0.33
20160927	24	ALM	17:01	-9.79	-10.45	1509	26.28	0.16	0.25
20160927	25	PPL	17:03	-9.76	-10.52	1513	80.60	0.27	0.25
Median	**N/A**	**Mode**	**Mean**	**Mean**	**Mean**	**Mean**	**Mean**	**Mean**	**Mean**
20160910		PPL	11:33	-15.88	7.94	1125	86.65	0.52	0.45

Table 2.2 – The 143 sky scans utilized from the ORACLES 2017 campaign.

Date	Scan No.	Scanning Method	Time (UTC)	Latitude (°)	Longitude (°)	Altitude (m)	Elevation Angle (°)	Flight Level Albedo	AOD (500nm)
20170812	97	PPL	12:00	-11.09	5.00	1185	107.76	0.66	0.24
20170812	100	PPL	12:02	-10.92	5.00	1212	108.25	0.70	0.22
20170812	121	PPL	13:18	-5.86	5.00	42	109.49	0.05	0.34
20170812	124	PPL	13:19	-5.75	5.00	41	105.71	0.04	0.32
20170812	127	PPL	13:21	-5.64	5.00	45	108.31	0.04	0.31
20170812	145	PPL	13:41	-4.17	5.00	1161	105.83	0.38	0.30
20170812	151	PPL	13:47	-3.71	5.00	1128	101.80	0.39	0.26
20170812	154	PPL	13:48	-3.62	5.00	1167	102.46	0.52	0.27
20170812	157	PPL	13:52	-3.40	5.00	1186	102.21	0.53	0.27
20170812	160	ALM	13:53	-3.29	5.00	1174	57.74	0.54	0.29
20170812	165	PPL	13:57	-2.98	5.00	1258	100.58	0.57	0.32
20170812	240	ALM	15:23	-0.77	5.00	2124	38.89	0.45	0.34
20170812	241	PPL	15:25	-0.69	5.00	2127	84.61	0.65	0.34
20170812	244	ALM	15:27	-0.48	5.00	2126	38.14	0.36	0.34
20170812	245	PPL	15:29	-0.40	5.00	2127	86.72	0.62	0.34
20170812	250	PPL	15:32	-0.19	5.00	2125	86.23	0.64	0.36
20170812	253	ALM	15:33	-0.05	5.00	2125	36.93	0.22	0.36
20170813	33	ALM	10:28	-8.82	4.85	1418	63.42	0.76	0.20
20170813	34	PPL	10:29	-8.74	4.84	1422	108.52	0.63	0.22
20170813	40	ALM	10:59	-7.02	4.46	1450	71.46	0.50	0.22
20170813	56	ALM	11:16	-8.12	4.70	1423	73.88	0.40	0.21
20170813	71	PPL	11:40	-9.08	4.91	1449	109.54	0.57	0.24
20170813	75	PPL	11:45	-8.67	4.82	1441	114.81	0.64	0.24
20170813	79	PPL	11:51	-8.23	4.73	1448	111.73	0.42	0.25
20170813	89	PPL	12:12	-6.74	4.40	1382	111.29	0.25	0.25
20170813	93	PPL	12:19	-6.25	4.30	1386	112.44	0.11	0.24
20170813	113	ALM	12:36	-6.58	4.37	47	71.32	0.05	0.45
20170813	120	PPL	12:48	-7.32	4.53	573	108.01	0.07	0.46
20170813	151	ALM	14:29	-7.95	4.66	1518	48.87	0.13	0.26
20170813	152	PPL	14:30	-8.02	4.68	1521	95.46	0.15	0.24
20170813	155	ALM	14:36	-8.41	4.77	1522	46.94	0.14	0.22
20170813	156	PPL	14:37	-8.49	4.78	1521	93.91	0.14	0.22
20170813	159	ALM	14:41	-8.74	4.84	1523	45.49	0.33	0.21
20170813	160	PPL	14:42	-8.82	4.85	1520	92.65	0.42	0.20
20170813	163	ALM	14:47	-8.86	4.86	1522	45.19	0.53	0.20
20170813	164	PPL	14:48	-8.78	4.85	1522	90.47	0.41	0.20
20170813	167	ALM	14:50	-8.67	4.82	1521	44.15	0.29	0.21
20170815	70	PPL	11:48	-13.63	5.00	853	111.01	0.15	0.43
20170815	96	PPL	12:05	-12.40	5.00	1959	107.75	0.26	0.41

Date	Scan No.	Scanning Method	Time (UTC)	Latitude (°)	Longitude (°)	Altitude (m)	Elevation Angle (°)	Flight Level Albedo	AOD (500nm)
20170815	99	PPL	12:07	-12.26	5.00	1959	108.96	0.26	0.43
20170815	102	PPL	12:10	-12.02	5.00	1959	109.00	0.31	0.45
20170815	103	PPL	12:12	-11.93	5.00	1960	107.85	0.32	0.45
20170815	104	PPL	12:14	-11.75	5.00	1959	107.66	0.35	0.45
20170815	105	PPL	12:17	-11.54	5.00	1959	109.06	0.25	0.45
20170815	106	PPL	12:19	-11.35	5.00	1959	109.18	0.42	0.47
20170815	110	PPL	12:25	-10.93	5.00	2492	109.25	0.39	0.35
20170815	113	PPL	12:28	-10.70	5.00	2489	108.01	0.33	0.38
20170815	114	PPL	12:30	-10.51	5.00	2490	107.85	0.33	0.38
20170815	117	PPL	12:33	-10.30	5.00	2490	108.93	0.34	0.37
20170815	120	ALM	12:36	-10.08	5.00	2490	67.68	0.31	0.36
20170815	121	ALM	12:39	-9.75	5.00	2491	67.74	0.36	0.30
20170815	124	PPL	12:44	-9.45	5.00	2490	107.30	0.32	0.23
20170815	127	ALM	12:47	-9.15	5.00	2488	67.56	0.32	0.21
20170817	86	PPL	13:07	-6.06	-4.56	1701	115.13	0.10	0.16
20170817	90	PPL	13:13	-5.73	-4.26	1200	113.52	0.08	0.23
20170817	94	PPL	13:16	-5.56	-4.10	1201	113.29	0.09	0.22
20170817	97	PPL	13:24	-5.19	-3.77	1707	112.12	0.09	0.15
20170817	100	PPL	13:44	-4.35	-3.31	1658	109.56	0.10	0.18
20170817	103	ALM	13:51	-4.78	-3.51	1736	65.00	0.10	0.20
20170817	104	PPL	13:52	-4.86	-3.55	1736	108.62	0.11	0.17
20170817	122	ALM	15:07	-8.01	-8.01	60	49.41	0.06	0.26
20170817	123	PPL	15:08	-8.01	-8.07	67	94.90	0.06	0.24
20170817	139	ALM	15:37	-8.01	-10.17	59	45.85	0.07	0.36
20170818	135	PPL	15:54	-8.21	-10.87	55	89.14	0.07	0.35
20170821	67	ALM	13:30	-8.00	-7.57	1384	72.43	0.08	0.24
20170821	68	PPL	13:32	-8.00	-7.50	1385	108.70	0.10	0.24
20170821	71	PPL	13:33	-8.00	-7.42	1378	108.54	0.15	0.23
20170821	77	PPL	13:41	-8.00	-6.94	1522	109.96	0.20	0.26
20170821	80	ALM	13:43	-8.00	-6.80	1667	69.54	0.49	0.27
20170821	84	ALM	13:45	-8.00	-6.64	1665	69.11	0.28	0.30
20170821	85	PPL	13:47	-8.00	-6.57	1662	109.78	0.19	0.29
20170821	88	ALM	13:58	-8.01	-5.69	2812	65.12	0.17	0.19
20170821	89	PPL	14:00	-8.01	-5.61	2816	106.58	0.25	0.19
20170821	92	ALM	14:01	-8.01	-5.46	2815	64.49	0.52	0.18
20170821	93	PPL	14:02	-8.01	-5.38	2816	104.70	0.59	0.19
20170821	105	ALM	16:09	-8.00	3.45	1253	29.02	0.74	0.73
20170821	106	PPL	16:11	-8.00	3.52	1253	77.45	0.25	0.74
20170821	109	ALM	16:18	-8.01	3.30	1384	26.04	0.66	0.70
20170821	110	PPL	16:19	-8.01	3.22	1383	72.62	0.27	0.71

Date	Scan No.	Scanning Method	Time (UTC)	Latitude (°)	Longitude (°)	Altitude (m)	Elevation Angle (°)	Flight Level Albedo	AOD (500nm)
20170821	114	PPL	16:22	-8.01	3.03	1387	73.35	0.76	0.70
20170821	150	ALM	16:46	-8.00	3.93	2724	19.26	0.65	0.32
20170821	151	PPL	16:47	-8.00	4.01	2724	69.63	0.53	0.28
20170821	154	ALM	16:48	-8.00	4.12	2726	18.65	0.42	0.28
20170821	155	PPL	16:50	-8.00	4.20	2726	68.89	0.66	0.29
20170821	158	ALM	16:51	-8.00	4.33	2727	17.64	0.57	0.27
20170821	159	PPL	16:53	-8.00	4.41	2727	68.08	0.27	0.27
20170821	162	ALM	16:54	-8.00	4.51	2726	16.90	0.49	0.24
20170821	163	PPL	16:56	-8.00	4.59	2725	67.34	0.62	0.23
20170824	13	PPL	11:46	-14.01	5.00	902	109.33	0.44	0.26
20170824	34	PPL	12:25	-11.45	5.00	1066	108.76	0.10	0.39
20170824	43	PPL	13:11	-8.49	5.00	1953	105.65	0.11	0.41
20170824	46	ALM	13:12	-8.37	5.00	1952	65.23	0.12	0.42
20170824	50	PPL	13:18	-7.99	5.00	1952	104.57	0.10	0.66
20170826	35	PPL	11:08	-5.25	5.06	975	116.90	0.07	0.34
20170826	39	PPL	11:10	-5.16	4.93	974	116.52	0.06	0.34
20170826	43	PPL	11:13	-5.07	4.79	973	114.42	0.13	0.36
20170826	47	PPL	11:25	-5.11	4.85	2167	117.35	0.10	0.20
20170826	51	PPL	11:28	-5.22	5.01	2167	118.14	0.15	0.18
20170828	19	PPL	11:31	-10.38	5.00	1123	114.76	0.21	0.55
20170828	23	PPL	11:34	-10.59	5.00	1122	114.40	0.17	0.54
20170828	27	PPL	11:39	-10.87	5.00	1122	114.30	0.28	0.48
20170828	44	PPL	12:12	-9.22	5.00	1229	115.50	0.52	0.58
20170828	51	PPL	12:28	-8.15	5.00	1290	111.25	0.32	0.75
20170828	55	PPL	12:31	-7.97	5.00	1342	113.51	0.40	0.75
20170828	62	PPL	12:52	-8.81	5.00	1139	109.21	0.36	0.66
20170828	65	ALM	12:54	-8.91	5.00	1167	69.08	0.29	0.53
20170828	71	ALM	13:05	-9.62	5.00	1339	66.43	0.52	0.59
20170828	72	PPL	13:06	-9.69	5.00	1341	106.52	0.38	0.49
20170828	97	ALM	14:50	-4.27	5.00	2726	45.39	0.71	0.50
20170828	98	PPL	14:51	-4.35	5.00	2725	90.54	0.62	0.45
20170828	101	ALM	14:59	-4.98	5.00	2726	42.43	0.30	0.49
20170828	102	PPL	15:00	-5.06	5.00	2726	90.32	0.18	0.48
20170828	105	ALM	15:06	-5.50	5.00	2726	40.79	0.42	0.40
20170828	106	PPL	15:07	-5.59	5.00	2726	87.40	0.16	0.45
20170830	63	ALM	13:47	-8.03	5.00	1359	59.03	0.50	1.36
20170830	68	ALM	14:20	-8.74	5.00	2431	51.87	0.47	0.92
20170830	69	PPL	14:22	-8.66	5.00	2431	98.03	0.51	0.92
20170830	72	ALM	14:28	-8.13	5.00	2429	49.46	0.51	0.80
20170830	73	PPL	14:30	-8.05	5.00	2430	94.80	0.49	0.87

Date	Scan No.	Scanning Method	Time (UTC)	Latitude (°)	Longitude (°)	Altitude (m)	Elevation Angle (°)	Flight Level Albedo	AOD (500nm)
20170831	17	ALM	10:34	-2.85	-0.94	2625	71.57	0.32	0.46
20170831	18	PPL	10:35	-2.93	-0.98	2625	112.51	0.42	0.46
20170831	22	PPL	10:42	-3.39	-1.25	2626	113.46	0.43	0.53
20170831	26	PPL	10:47	-3.74	-1.46	2625	114.18	0.15	0.58
20170831	30	PPL	10:58	-4.46	-1.88	2702	115.27	0.19	0.74
20170831	34	PPL	11:19	-5.90	-1.88	2764	117.72	0.60	0.79
20170831	38	PPL	11:27	-6.41	-1.69	2764	118.39	0.45	0.87
20170831	42	PPL	11:48	-7.94	-1.13	2917	118.01	0.11	0.69
20170831	46	PPL	12:17	-7.64	-1.24	2804	117.55	0.42	0.71
20170831	50	PPL	12:27	-6.86	-1.53	2803	117.81	0.35	0.75
20170831	54	PPL	12:39	-5.94	-1.86	2804	117.76	0.46	0.80
20170831	58	PPL	13:00	-4.41	-1.85	2430	117.61	0.56	0.84
20170831	62	PPL	13:15	-3.46	-1.29	1390	114.35	0.12	0.81
20170831	68	PPL	13:34	-2.26	-0.59	2441	111.70	0.32	0.62
20170831	71	ALM	13:56	-1.35	-0.15	2584	63.96	0.15	0.45
20170831	72	PPL	13:58	-1.43	-0.19	2584	107.79	0.14	0.47
20170831	75	ALM	14:27	-0.94	0.30	2734	57.81	0.13	0.38
20170831	76	PPL	14:28	-0.92	0.39	2735	102.62	0.13	0.37
20170902	12	PPL	11:37	0.00	-1.72	2147	122.16	0.64	0.24
20170902	40	ALM	15:10	-3.91	-12.14	1976	57.89	0.17	0.43
20170902	41	PPL	15:11	-3.98	-12.18	1978	102.67	0.10	0.42
20170902	44	ALM	15:13	-4.09	-12.24	1979	57.06	0.11	0.39
20170902	45	PPL	15:14	-4.16	-12.28	1977	102.31	0.10	0.42
20170902	60	PPL	16:28	-5.57	-13.06	1959	90.63	0.42	0.28
Median	**N/A**	**Mode**	**Mean**	**Mean**	**Mean**	**Mean**	**Mean**	**Mean**	**Mean**
20170821		PPL	13:33	-6.99	1.72	1813	88.75	0.33	0.40

Table 2.3 – The 83 sky scans utilized from the ORACLES 2018 campaign.

Date	Scan No.	Scanning Method	Time (UTC)	Latitude (°)	Longitude (°)	Altitude (m)	Elevation Angle (°)	Flight Level Albedo	AOD (500nm)
20180930	22	PPL	10:07	-7.82	5.00	856	113.87	0.26	0.33
20180930	26	PPL	10:10	-7.65	5.00	858	113.43	0.44	0.32
20180930	30	PPL	10:13	-7.46	5.00	858	116.36	0.39	0.35
20180930	34	PPL	10:16	-7.26	5.00	854	117.99	0.40	0.37
20181005	17	PPL	7:38	-9.50	6.23	885	87.51	0.33	0.31
20181005	18	ALM	7:39	-9.50	6.16	885	40.88	0.22	0.31
20181005	21	PPL	7:40	-9.50	6.06	885	88.09	0.21	0.31
20181005	22	ALM	7:41	-9.50	5.99	885	41.43	0.11	0.30
20181005	25	PPL	7:43	-9.50	5.91	885	88.51	0.11	0.31
20181005	28	PPL	7:45	-9.50	5.76	886	88.85	0.16	0.29
20181005	45	PPL	8:16	-9.50	6.07	337	95.39	0.08	0.39
20181005	48	PPL	8:19	-9.50	5.93	338	95.68	0.08	0.39
20181005	54	PPL	8:25	-9.50	5.87	837	94.58	0.24	0.33
20181005	55	ALM	8:26	-9.50	5.94	837	48.55	0.10	0.31
20181005	58	PPL	8:30	-9.50	6.16	1335	97.16	0.29	0.30
20181005	59	ALM	8:31	-9.50	6.24	1336	51.03	0.37	0.29
20181005	63	ALM	8:33	-9.50	6.43	1335	51.92	0.32	0.30
20181005	66	PPL	8:37	-9.50	6.71	1335	99.15	0.22	0.30
20181005	67	ALM	8:38	-9.51	6.79	1335	53.42	0.35	0.30
20181005	70	PPL	8:50	-9.50	6.52	2103	102.01	0.23	0.21
20181005	74	PPL	8:53	-9.50	6.23	2103	103.94	0.42	0.21
20181005	75	ALM	8:54	-9.50	6.14	2103	59.13	0.23	0.19
20181005	89	PPL	10:19	-9.54	5.84	526	118.59	0.07	0.35
20181007	33	PPL	11:14	-11.03	5.00	896	125.11	0.37	0.44
20181007	36	PPL	11:16	-10.96	5.00	898	125.80	0.28	0.45
20181007	39	PPL	11:17	-10.86	5.00	899	125.74	0.40	0.43
20181007	48	PPL	11:45	-8.94	5.00	2305	128.07	0.10	0.20
20181007	51	PPL	11:46	-8.84	5.00	2305	127.70	0.10	0.17
20181007	54	PPL	11:48	-8.73	5.00	2303	127.67	0.10	0.23
20181007	60	PPL	11:51	-8.51	5.00	2304	125.78	0.10	0.19
20181007	66	PPL	11:53	-8.32	5.00	2304	126.53	0.20	0.19
20181007	69	PPL	11:54	-8.22	5.00	2305	124.91	0.24	0.19
20181007	72	PPL	11:56	-8.13	5.00	2304	126.25	0.25	0.18
20181007	82	PPL	12:49	-9.01	5.00	53	112.05	0.06	0.36
20181010	28	PPL	10:27	-12.95	5.00	1062	120.60	0.60	0.45
20181010	31	PPL	10:28	-12.87	5.00	1064	115.46	0.50	0.48
20181010	34	PPL	10:29	-12.79	5.00	1067	117.47	0.53	0.48
20181010	37	PPL	10:31	-12.68	5.00	1061	116.37	0.37	0.48
20181010	67	PPL	11:34	-9.75	5.00	1338	126.26	0.27	0.35

Date	Scan No.	Scanning Method	Time (UTC)	Latitude (°)	Longitude (°)	Altitude (m)	Elevation Angle (°)	Flight Level Albedo	AOD (500nm)
20181010	76	PPL	11:37	-9.57	5.00	1337	126.06	0.38	0.32
20181010	95	PPL	11:58	-8.17	5.00	1149	125.67	0.08	0.31
20181010	98	PPL	12:05	-7.72	5.00	145	124.57	0.05	0.47
20181010	107	PPL	12:33	-5.83	5.00	1085	117.41	0.19	0.34
20181010	125	PPL	14:01	-2.51	5.00	559	100.41	0.08	0.44
20181010	128	PPL	14:02	-2.40	5.00	555	99.81	0.08	0.44
20181012	43	ALM	14:07	-2.01	6.51	1570	51.47	0.47	0.18
20181012	52	PPL	16:01	-3.83	5.50	1499	75.05	0.56	0.31
20181012	53	ALM	16:02	-3.75	5.50	1526	26.78	0.56	0.31
20181015	44	PPL	11:00	-12.37	5.00	1134	123.78	0.45	0.31
20181015	71	PPL	11:30	-10.44	5.00	1636	129.75	0.57	0.19
20181015	86	PPL	11:51	-9.50	5.00	1136	129.63	0.57	0.24
20181015	109	PPL	12:22	-7.58	5.00	1127	119.96	0.46	0.28
20181015	113	PPL	12:29	-7.15	5.00	2133	120.18	0.33	0.19
20181015	117	PPL	12:34	-6.75	5.00	2134	118.94	0.44	0.16
20181017	74	PPL	9:57	-7.51	10.50	1897	121.38	0.24	0.41
20181017	77	PPL	9:59	-7.43	10.50	1899	118.57	0.37	0.39
20181017	80	PPL	10:00	-7.33	10.50	1897	122.23	0.39	0.44
20181017	83	PPL	10:02	-7.22	10.50	1900	121.43	0.27	0.37
20181017	86	PPL	10:03	-7.13	10.50	1898	121.79	0.22	0.44
20181017	90	PPL	10:10	-7.06	10.50	1522	121.69	0.16	0.77
20181017	93	PPL	10:11	-7.17	10.50	1519	120.76	0.25	0.62
20181017	96	PPL	10:13	-7.26	10.50	1520	121.36	0.33	0.57
20181017	99	PPL	10:14	-7.36	10.50	1523	123.42	0.41	0.63
20181017	102	PPL	10:16	-7.44	10.50	1521	121.47	0.38	0.51
20181019	44	PPL	9:36	-7.78	9.00	70	116.62	0.05	0.33
20181019	48	PPL	9:39	-7.58	9.00	64	114.56	0.05	0.30
20181019	51	PPL	9:40	-7.50	9.00	68	113.47	0.05	0.31
20181019	59	PPL	9:50	-7.31	9.00	612	114.74	0.06	0.25
20181019	62	PPL	9:51	-7.40	9.00	611	118.22	0.07	0.24
20181019	65	PPL	9:53	-7.51	9.00	673	117.02	0.07	0.25
20181019	68	PPL	9:54	-7.59	9.00	666	117.45	0.07	0.25
20181019	72	PPL	9:57	-7.78	9.00	668	116.01	0.07	0.26
20181019	75	PPL	9:59	-7.88	9.00	667	120.11	0.07	0.27
20181019	78	PPL	10:10	-8.02	9.00	2425	122.65	0.09	0.26
20181019	81	PPL	10:12	-7.90	9.00	2424	121.49	0.09	0.22
20181019	85	PPL	10:15	-7.67	9.00	2424	122.84	0.10	0.23
20181019	88	PPL	10:17	-7.58	9.00	2424	121.84	0.10	0.21
20181019	113	PPL	12:08	-7.78	9.00	836	120.07	0.12	0.27
20181019	116	PPL	12:09	-7.71	9.00	844	118.90	0.16	0.26

Date	Scan No.	Scanning Method	Time (UTC)	Latitude (°)	Longitude (°)	Altitude (m)	Elevation Angle (°)	Flight Level Albedo	AOD (500nm)
20181019	119	PPL	12:10	-7.63	9.00	957	120.08	0.35	0.24
20181019	122	PPL	12:12	-7.53	9.00	1028	120.52	0.43	0.24
20181019	128	PPL	12:38	-7.29	9.00	1097	114.34	0.52	0.24
20181021	55	PPL	10:46	-12.24	5.00	854	122.78	0.34	0.26
Median	**N/A**	**Mode**	**Mean**	**Mean**	**Mean**	**Mean**	**Mean**	**Mean**	**Mean**
20181010		PPL	10:35	-8.38	6.82	1257	108.39	0.26	0.32

2.5 – AAE Calculation

Following sky scan retrieval, the final property left to determine manually is AAE. For this thesis work, both linear AAE and quadratic AAE are used. The linear AAE meets the most common definition of AAE and can establish the dominant aerosol type (Russell et al., 2010). To calculate this, the linear regression of logarithmic AAOD over logarithmic wavelength is taken, with the resultant slope being the linear AAE.

The quadratic AAE will display any spectral changes in AAE and can speak to any evolution in the mix of aerosol types (Bond et al., 2013), if present. The quadratic AAE will clarify if aerosol absorption is uniform (presence of BC), strong in the shorter wavelengths (presence of BrC), or strong in the longer wavelengths (presence of mineral dust). To calculate this, a quadratic regression of logarithmic AAOD over logarithmic wavelength is taken. The first derivative of this quadratic regression at the wavelength set of 500, 675, 870, 995 nm gives the tangential slopes that represent the quadratic AAE at those wavelengths.

2.6 – Subseasonal Analysis

With all the pertinent radiative properties now calculated, a subseasonal analysis was then conducted on SSA, AOD, AAOD, linear AAE, and quadratic AAE. Sky scans meeting QA/QC criteria were grouped by ORACLES campaign year. Boxplots were then created via MATLAB to compare all three campaigns for each radiative property at each of the four wavelengths. The radiative properties are presented by month (08/2017, 09/2016, 10/2018), instead of by ORACLES campaign year, so that the subseasonal variability across the campaigns is apparent. The radiative properties are also grouped by wavelength, which is denoted by different colors, so that the spectral dependence within each campaign is also visible.

The subseasonal analysis will unveil changes in scattering/absorption (SSA and AAOD), changes in aerosol loading (AOD), and changes in aerosol type (AAE). The magnitude of the subseasonal variability in SSA will have implications for radiative flux calculations over the SE Atlantic (Russell et al., 2002). The subseasonal variability in AAE will reveal if the changes in scattering/absorption are due to the mix of aerosol types (Bond et al., 2013) or the evolution of BB aerosol composition (Eck et al., 2013). This analysis will also allow for the comparison of the subseasonal variability of SSA and AOD from the ORACLES 2016-2018 campaigns against that of the extended AERONET 1995-2013 record (Redemann et al., 2021).

Chapter 3 – Results

3.1 – SSA

The subseasonal variability of SSA (Figure 3.1) was found to be an upward curving trend. The SSA median falls about 0.01 – 0.02 from August to September (indicating a slight decrease in the proportion of scattering relative to extinction), followed by a rise of about 0.04 – 0.06 by October (indicating a sharper increase in the proportion of scattering). This subseasonal trend holds true at all four wavelengths, with the greatest magnitude at 500 nm, but that magnitude then decreases with increasing wavelength. All three campaigns have their smallest value ranges at 500 nm, but the value ranges of the 2017 and 2018 campaigns are much larger at longer wavelengths. These variations in SSA are suggestive of subseasonal changes in aerosol scattering, with the SSA differences (especially between September and October) being great enough to considerably affect aerosol-induced radiative flux (Russell et al., 2002). The spectral SSA medians from the 2016 campaign align well with Figure 11 from Pistone et al. (2019).

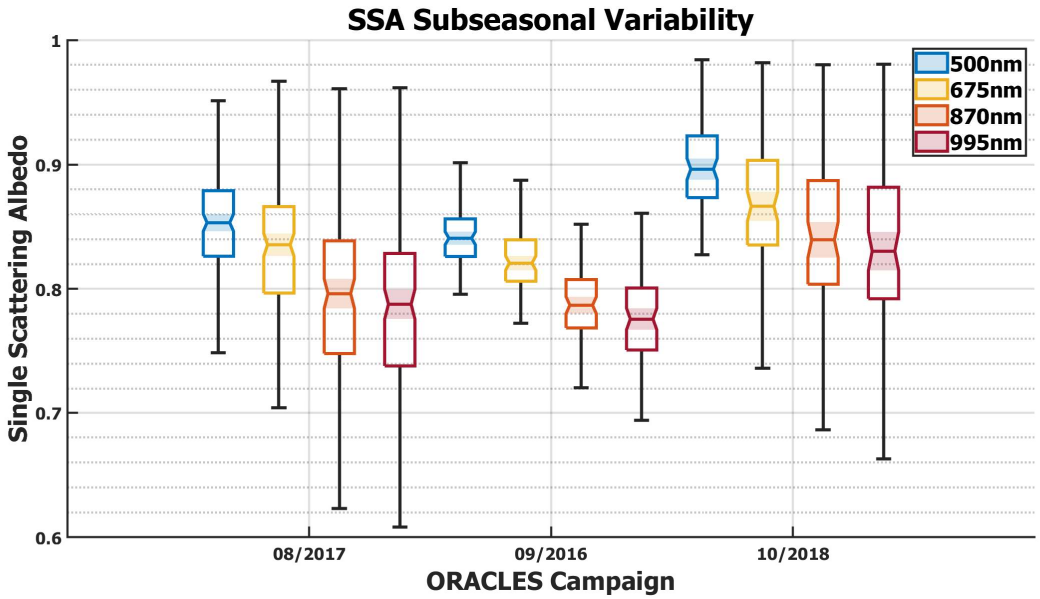

Figure 3.1 – Subseasonal variability of SSA.

3.2 – AOD

The subseasonal variability of AOD is a downward curving trend, with the AOD median increasing between August and September and then experiencing a slightly sharper decrease by October. The subseasonal trend holds across all wavelengths. The 2018 campaign consistently has the smallest AOD value range at all four wavelengths. These results suggest that aerosol loading over the SE Atlantic is at its peak in September, with less aerosol loading in August and an even lower aerosol loading in October.

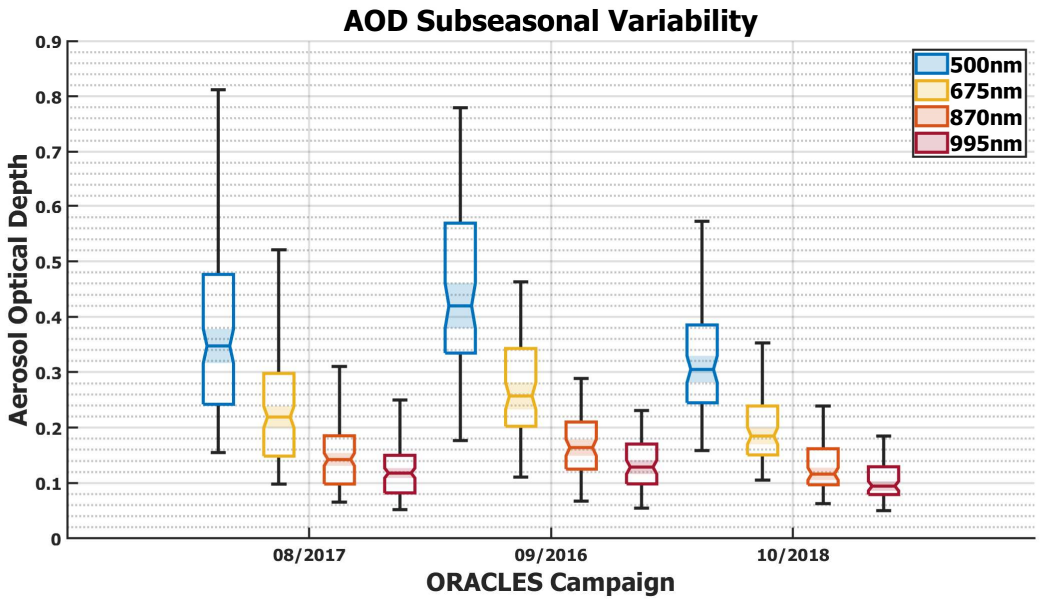

Figure 3.2 – Subseasonal variability of AOD.

3.3 – AAOD

The subseasonal variability of AAOD is also a downward curving trend, with the AAOD median increasing between August and September followed by a larger decrease by October. This subseasonal trend holds for all four wavelengths, with the greatest magnitude at 500 nm, but that magnitude then decreases with increasing wavelength. As was observed with AOD, the 2018 campaign again has the smallest AAOD value range across all four wavelengths. The subseasonal trend indicates that aerosol absorption greatly decreases between September and October, which reaffirms the concurrent trend in SSA that showed a sharp increase in aerosol scattering at that time.

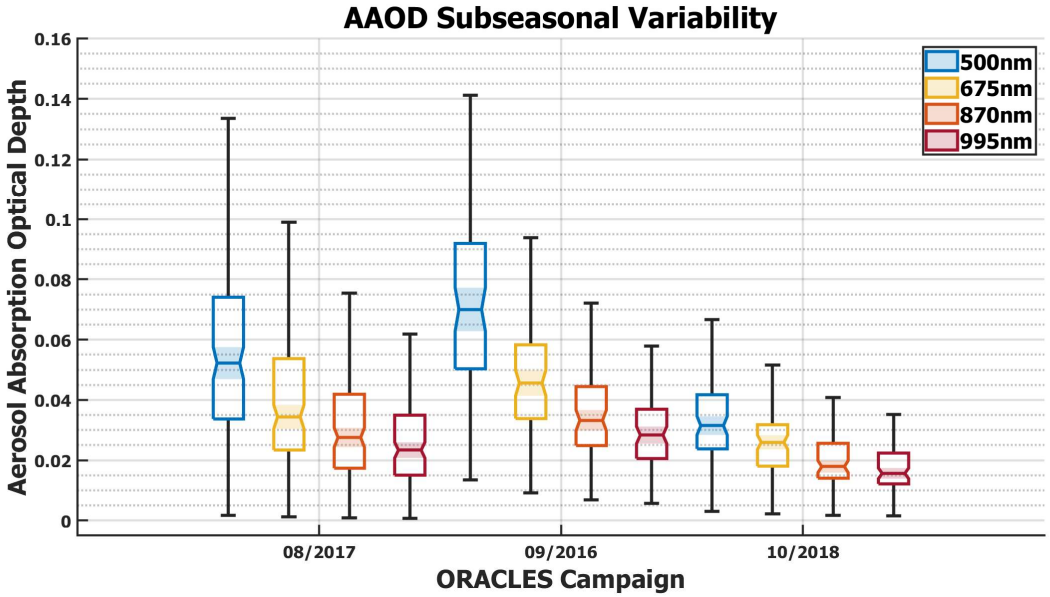

Figure 3.3 – Subseasonal variability of AAOD.

3.4 – Linear AAE

The subseasonal variability of linear AAE is another downward curving trend, with the AAE median rising from about 1.1 in August to about 1.25 in September (an increase of 0.15), and then falling to about 1.0 by October (a decrease of 0.25). All three campaigns have an AAE value range of about 1.0, with the vast majority of AAE values located between 0.5 and 1.5. By AAE continuing the trend found in AAOD, it is now shown that a subseasonal variation in aerosol absorption is occurring, independent of aerosol loading. The centering of the AAE medians near 1.0 suggests the predominance of BC aerosols throughout the season (Russell et al., 2010).

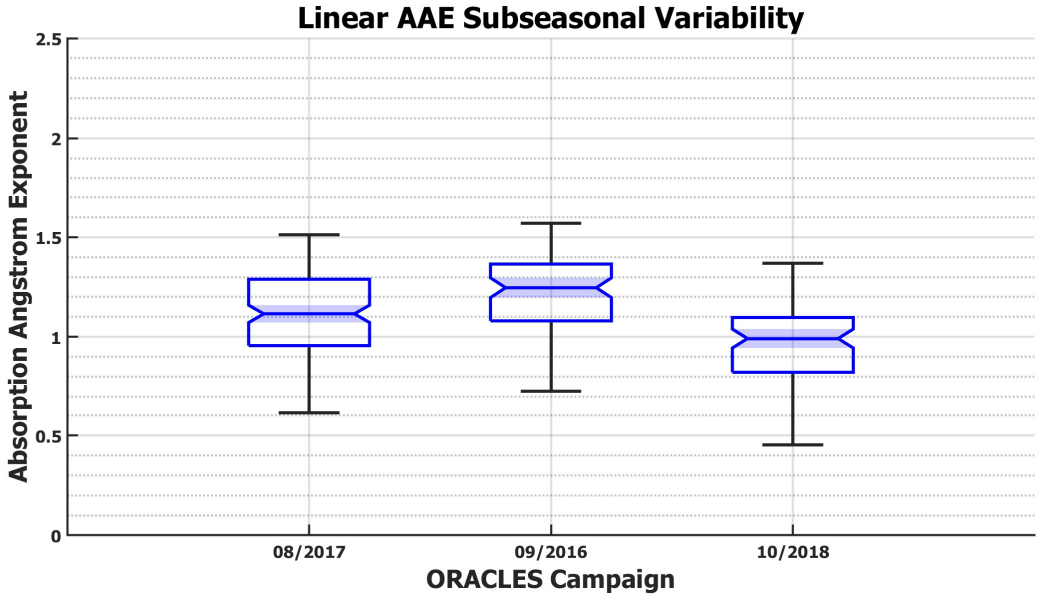

Figure 3.4 – Subseasonal variability of linear AAE.

3.5 – Quadratic AAE

The subseasonal variability of quadratic AAE is yet another downward curving trend, with the AAE median increasing between August and September and then decreasing by October. The subseasonal variability of quadratic AAE is spectrally dependent, with the subseasonal trend apparent at 500 and 675 nm, but nearly nonexistent at 870 and 995 nm. This is largely a function of the shorter wavelengths "bounding" the quadratic regression, allowing for greater variability. Like with linear AAE, the value ranges are also centered between 0.5 and 1.5, but the value ranges are considerably larger than 1.0 at all wavelengths except 675 nm. The smallest value ranges for all three campaigns are found at 675 nm. This is a function of the quadratic AAE calculations, as the median value (and thus the closest to the linear AAE) is heavily centered towards 675 nm, resulting in the best agreement at that wavelength. The lack of a strong absorption in the short wavelengths indicates an absence of BrC aerosols, while the lack of strong absorption in the long wavelengths also indicates an absence of mineral dust aerosols.

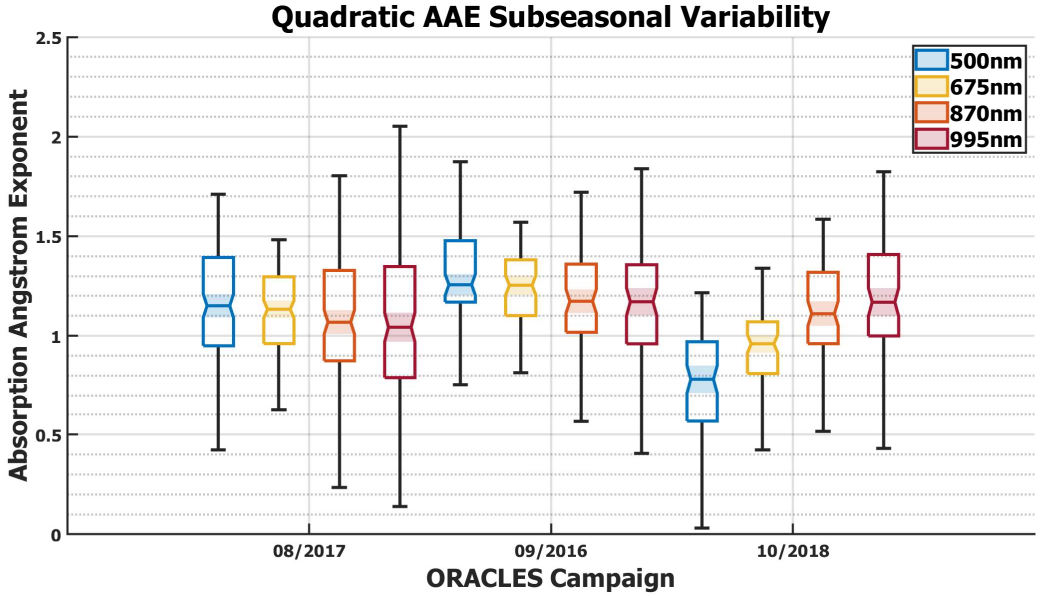

Figure 3.5 – Subseasonal variability of quadratic AAE.

Chapter 4 – Discussion

4.1 – Subseasonal Variability of the Aerosol Radiative Properties

By considering all the above radiative properties together, a cohesive story regarding the subseasonal variability of aerosols over the SE Atlantic emerges. A rise in SSA of 0.04 – 0.06 from September to October is a significant increase in the proportion of aerosol scattering, and properly accounting for it is useful for accurately determining aerosol-induced radiative flux (Russell et al., 2002). AOD shows that aerosol loading reaches its peak in September and sharply decreases by October. AAOD displays a sharp decrease from September to October, which echoes the concurrent and opposite increase in SSA, confirming a subseasonal change in aerosol scattering/absorption. The centering of linear AAE near 1.0, coupled with its small value ranges, indicates that BC aerosols dominate throughout the season. This is supported by the quadratic AAE, with its spectral uniformity suggesting a lack of significant BrC or mineral dust aerosols. Since it appears that there is not a notable change in the mix of aerosol types during the season, then the subseasonal change in scattering/absorption is most likely due to a change in BB aerosol composition (Eck et al., 2013).

4.2 – ORACLES vs. AERONET

In general, the subseasonal variability of aerosols observed by ORACLES over the study region of the SE Atlantic is in good agreement with the observations by AERONET in the source region of Southern Africa (Redemann et al., 2021). In both regions, there is an upward curving trend in SSA during the BB emission season (Figure 4.1). One difference is that SSA appears to reach a minimum in early August in Southern Africa, but it does not reach a minimum until September over the SE Atlantic. Less AERONET data is available for July than the other months, implying that the drop in the median SSA may not be as steep as it appears. However, assuming that it is accurate, aerosol transport alone cannot account for the temporal difference between the two minimums, as aerosol transport should only take up to 10 days (Adebiyi & Zuidema, 2016), whereas the minimums have a difference of about 35 days. As such, I posit that this is largely a function of the differing latitudes of the three ORACLES campaigns, as the 08/2017 campaign (mean of 6.99°S) and 10/2018 campaign (mean of 8.38°S) are much closer to the centroid of the aerosol smoke plume (Redemann et al., 2021) and thus the AERONET median, whereas the 09/2016 campaign (mean of 15.88°S), is further south and better aligns with the AERONET stations near 15°S.

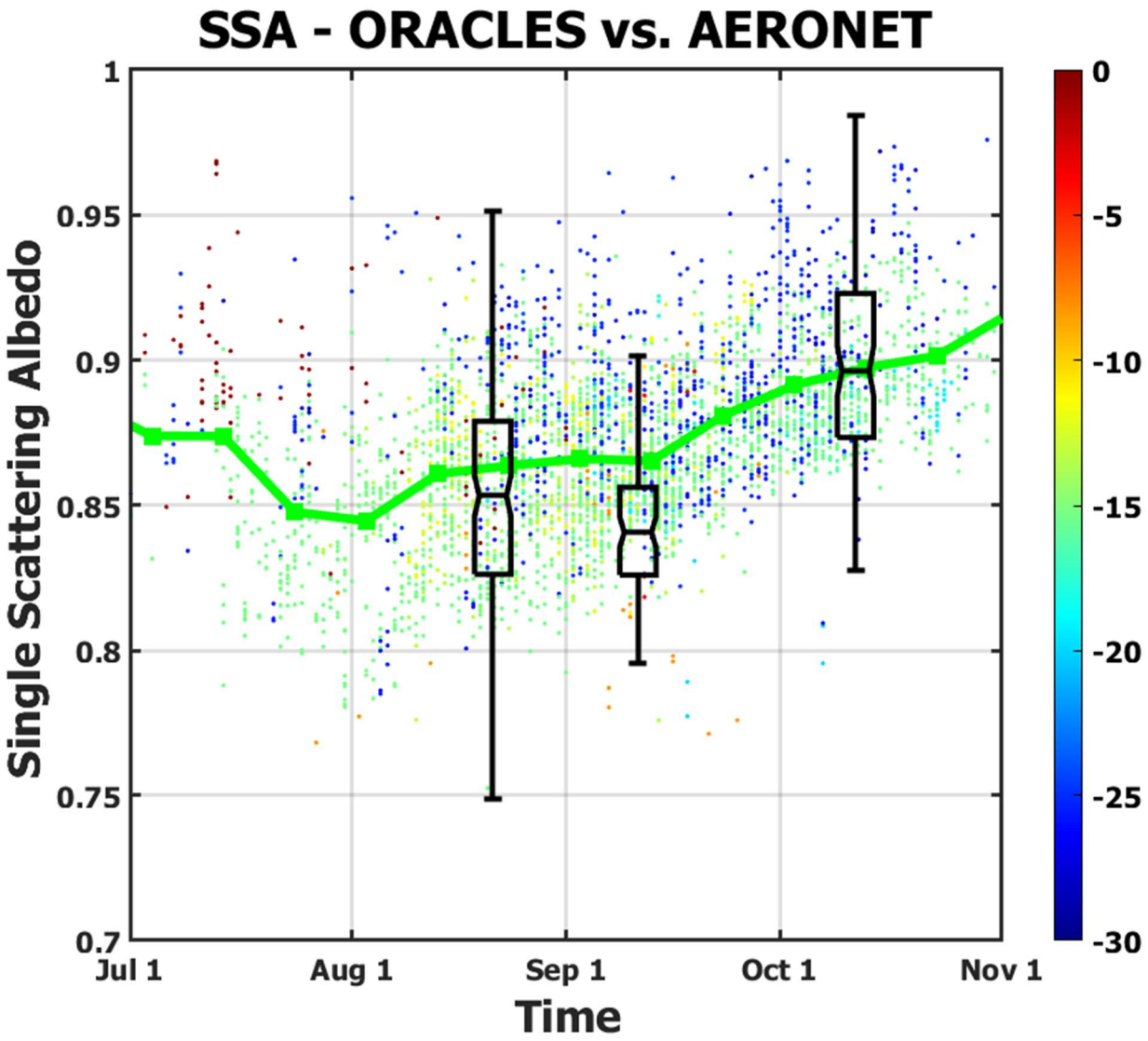

Figure 4.1 – Subseasonal variability of SSA for ORACLES (2016-2018) at 500 nm (black) vs. AERONET (1995-2013) at 440 nm (green).

Both regions also share a downward curving trend in AOD during the BB emission season (Figure 4.2). In both cases, AOD increases from August to September (reaching its peak) and then decreases from September to October. Here, the timing of the subseasonal trends align better than with SSA, such that the only apparent issue is that the AOD medians from ORACLES are consistently lower than those from AERONET. This might be related to the distance between the source region and the measurements, but also could be a function of the difference between the two wavelengths being compared, as the AOD from ORACLES is at 500 nm, whereas the AOD from AERONET is at 440 nm. We would expect the AOD at 500 nm to be lower than at 440 nm, so this discrepancy makes sense. In the future, this can be explicitly resolved by using EAE to extrapolate the AOD from ORACLES at 500 nm to 440 nm, so that the comparison is more one-to-one. Even though this issue was not as apparent in the SSA comparison, it would also benefit from such an extrapolation.

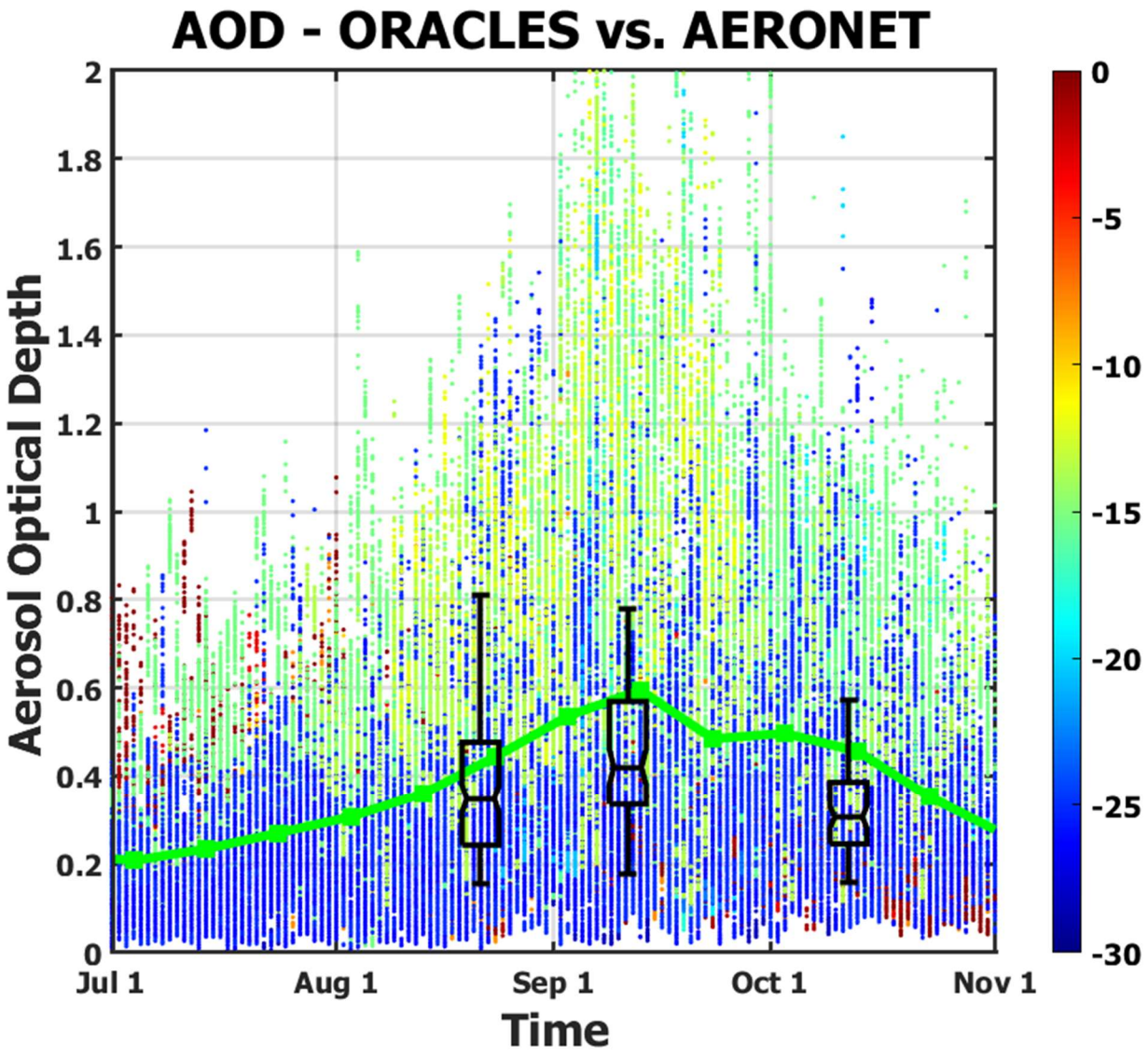

Figure 4.2 – Subseasonal variability of AOD for ORACLES (2016-2018) at 500 nm (black) vs. AERONET (1995-2013) at 440 nm (green).

Despite some differences in the fine details, the subseasonal variability of aerosol radiative properties retrieved by ORACLES are broadly consistent in key features with those retrieved by AERONET. This shows that 4STAR provides reliable airborne retrievals that can effectively fill gaps in ground-based AERONET coverage. The analysis also bridges the spatial differences between the downstream study region of the SE Atlantic and the upstream source region of Southern Africa, indicating that radiative properties are conserved well enough during short-term BB aerosol transport for measurements from one region to be representative of the other. It also shows a temporal continuation in the ORACLES 2016-2018 campaigns of the subseasonal trend already found in the extended AERONET 1995-2013 record.

Chapter 5 – Conclusion

5.1 – Key Takeaways

SSA subseasonal variability shows that the proportion of scattering increases from September to October over the SE Atlantic. This, paired with a concurrent decrease in AAOD, reveals that a significant change in aerosol scattering/absorption is occurring, a finding which impacts the calculation of aerosol-induced radiative flux (Russell et al., 2002). The relatively small magnitude of change in AAE indicates that the mix of aerosol types remains dominated by BC aerosols throughout the season, with few BrC or mineral dust aerosols present (Russell et al., 2010). Thus, this subseasonal trend in aerosol scattering/absorption is likely attributable to an evolution in BB aerosol composition. This hypothesis can be confirmed by examining the change in the imaginary refractive index throughout the BB emission season (Eck et al., 2013).

Comparing ORACLES retrievals against those from AERONET reveals strong agreement regarding the subseasonal variability of aerosol radiative properties, which is remarkable given the differences in methodology, study area, and temporal extent. This agreement shows that 4STAR provides reliable airborne retrievals that can fill gaps in ground-based AERONET coverage. The analysis also opens the door to future comparisons between other downwind study areas and their upwind source regions, as the aerosol radiative properties are well conserved during the short-term BB aerosol transport from Southern Africa to the SE Atlantic. Finally, it places the ORACLES 2016-2018 campaigns in context of the extended AERONET 1995-2013 record, showing a temporal continuation of existing subseasonal trends.

The method for wavelength selection employed by this thesis has also allowed us to create the first ever complete set of ORACLES/4STAR 2016-2018 sky scans for data archival.

The use of a four-wavelength set of 500, 675, 870, and 995 nm made possible the accurate retrieval of aerosol radiative properties while avoiding an instrument artifact that affected the 2017 and 2018 campaigns. It also avoids the issue of stray light scattering that was found to affect the ultraviolet wavelengths, although future efforts can be made to correct for both issues, which would extend the range of 4STAR retrievals, strengthen inter-instrumental comparisons, and improve the analysis of aerosol type.

5.2 – Future Work

Future work could include the running of 4STAR sky scans through GRASP (Generalized Retrieval of Aerosol and Surface Properties) retrieval code. GRASP is better suited to make use of 4STAR hyperspectral measurements than the current AERONET code adapted for this study as it can produce retrievals at hundreds of wavelengths. The current AERONET-adapted code, in contrast, is limited to discrete spectral measurements, lest the retrieval fail to converge on a realistic result. In addition to resolving this spectral limitation issue, GRASP's hyperspectral capabilities have the potential to simultaneously retrieve trace gas concentrations, commensurately improve AOD and AAOD spectrum, diagnose stray light scattering, and resolve the instrument artifact issue.

Another possibility includes the examination of the subseasonal variability of imaginary refractive index, which will test the hypothesis that the changes in aerosol scattering/absorption are due to an evolution in BB aerosol composition (Eck et al., 2013). The subseasonal variability of aerosol size distribution, the other core retrieval variable, can also be analyzed, which might show differences in the smoke plumes observed during each campaign. These retrieval variables will provide additional information that can help to improve our understanding of aerosol-cloud-radiation interactions with the semipermanent subtropical stratocumulus cloud deck.

Besides ORACLES, 4STAR was also used in other airborne campaigns, including SEAC4RS and TCAP. As such, a similar methodology to that employed by this thesis can be used to compile complete sets of 4STAR sky scans for those campaigns as well, allowing for inter-campaign comparisons between the three projects. Each of these campaigns can also be compared against their nearby AERONET stations, which will speak to the value added by each airborne campaign to their respective regions.

5.3 – Environmental Implications

A final consideration is how this research could be useful to relevant policymakers and stakeholders in Southern Africa. As has been discussed throughout this thesis, the net effect of BB aerosols on climate is not totally clear, as radiative absorption by BC aerosols causes warming, while contributions to a stratocumulus cloud deck causes cooling, and the radiative properties of these BB aerosols will vary from month to month. As such, it can't be definitively stated what the impact of policies aimed at reducing BB aerosol emissions would have on the people of Southern Africa. However, given the negative effects that BB aerosols can have on human health, all relevant factors should be considered.

Two of the major contributors to BB aerosol emissions in Southern Africa are forest/savannah BB and residential BB. With forest/savannah BB, the economic and nutritional benefits of new farmland must be weighed against air pollution and losses in biodiversity. BB emissions due to deforestation must also be considered separately from natural wildfires and controlled burn tactics, should such data be available. For residential BB, the prominence of traditional outdoor cooking methods must be taken into consideration, as reactionary legislation that ignores the customs and perspectives of local peoples will fail to bring substantive and equitable change. Finally, although we must strive as a united world to resolve climate change and global health issues, the topic of climate justice cannot be avoided, as developing nations in Africa should not be expected to bear the heaviest economic burden from new environmental policies, just because developed nations have already been able to enjoy the full fruits of industrialization.

References

Adebiyi, A. A., & Zuidema, P. (2016). The role of the southern African easterly jet in modifying the southeast Atlantic aerosol and cloud environments, *Quarterly Journal of the Royal Meteorological Society*, 142, 1574–1589. https://doi.org/10.1002/qj.2765

Albrecht, B. A. (1989). Aerosols, cloud microphysics, and fractional cloudiness. *Science, 245*(4923), 1227-1230. https://doi.org/10.1126/science.245.4923.1227

Allen, R. J., Amiri-Farahani, A., Lamarque, J. F., Smith, C., Shindell, D., Hassan, T., & Chung, C. E. (2019). Observationally constrained aerosol–cloud semi-direct effects. *npj Climate and Atmospheric Science*, *2*(1), 1-12. https://doi.org/10.1038/s41612-019-0073-9

Andreae, M. O., & Rosenfeld, D. (2008). Aerosol–cloud–precipitation interactions: Part 1: The nature and sources of cloud-active aerosols. *Earth-Science Reviews*, *89*(1-2), 13-41. https://doi.org/10.1016/j.earscirev.2008.03.001

Bergstrom, R. W., Pilewskie, P., Schmid, B., & Russell, P. B. (2003). Estimates of the spectral aerosol single scattering albedo and aerosol radiative effects during SAFARI 2000. *Journal of Geophysical Research: Atmospheres*, *108*(D13). https://doi.org/10.1029/2002JD002435

Bi, L., Yang, P., Kattawar, G. W., & Kahn, R. (2009). Single-scattering properties of triaxial ellipsoidal particles for a size parameter range from the Rayleigh to geometric-optics regimes. *Applied Optics*, *48*(1), 114-126. https://doi.org/10.1364/AO.48.000114

Bond, T. C., Doherty, S. J., Fahey, D. W., Forster, P. M., Berntsen, T., DeAngelo, B. J., et al. (2013). Bounding the role of black carbon in the climate system: A scientific assessment. *Journal of Geophysical Research: Atmospheres*, *118*(11), 5380-5552. https://doi.org/10.1002/jgrd.50171

Boucher, O., Randall, D., Artaxo, P., Bretherton, C., Feingold, G., Forster, P., et al. (2013). Chapter 7: Clouds and aerosols. In T. F. Stocker, et al. (Eds.), *Climate Change 2013: The physical science basis: Contribution of Working Group I to the Fifth Assessment Report of the Intergovernmental Panel on Climate Change* (pp. 571–657). Cambridge, UK & New York, NY: Cambridge University Press. https://doi.org/10.1017/CBO9781107415324.016

Cappa, C., Kotamarthi, R., Selacek, A., Flynn, C., Lewis, E., McComiskey, A., & Riemer, N. (2016). *Absorbing Aerosols Workshop Report: January 20–21, 2016*. Washington, DC: U.S. Department of Energy. https://doi.org/10.2172/1471231

Charlson, R. J., & Pilat, M. J. (1969). Climate: The influence of aerosols. *Journal of Applied Meteorology and Climatology*, *8*(6), 1001-1002. https://doi.org/10.1175/1520-0450(1969)008<1001:CTIOA>2.0.CO;2

Cochrane, S. P., Schmidt, K. S., Chen, H., Pilewskie, P., Kittelman, S., Redemann, J., et al. (2022). Biomass burning aerosol heating rates from the ORACLES (ObseRvations of Aerosols above CLouds and their intEractionS) 2016 and 2017 experiments. *Atmospheric Measurement Techniques*, *15*(1), 61-77. https://doi.org/10.5194/amt-15-61-2022

Dubovik, O., Smirnov, A., Holben, B. N., King, M. D., Kaufman, Y. J., Eck, T. F., & Slutsker, I. (2000). Accuracy assessments of aerosol optical properties retrieved from Aerosol Robotic Network (AERONET) sun and sky radiance measurements. *Journal of Geophysical Research: Atmospheres*, *105*(D8), 9791-9806. https://doi.org/10.1029/2000JD900040

Dunagan, S. E., Johnson, R., Zavaleta, J., Russell, P. B., Schmid, B., Flynn, C., et al. (2013). Spectrometer for sky-scanning sun-tracking atmospheric research (4STAR): Instrument technology. *Remote Sensing*, *5*(8), 3872-3895. https://doi.org/10.3390/rs5083872

Eck, T. F., Holben, B. N., Reid, J. S., Mukelabai, M. M., Piketh, S. J., Torres, O., et al. (2013). A seasonal trend of single scattering albedo in southern African biomass-burning particles: Implications for satellite products and estimates of emissions for the world's largest biomass-burning source. *Journal of Geophysical Research: Atmospheres*, *118*(12), 6414-6432. https://doi.org/10.1002/jgrd.50500

Forster, P., Storelvmo, T., Armour, K., Collins, W., Dufresne, J. -L., Frame, D., et al. (2021). Chapter 7: The Earth's energy budget, climate feedbacks, and climate sensitivity. In V. Masson-Delmotte, et al. (Eds.), *Climate Change 2021: The physical science basis: Contribution of Working Group I to the Sixth Assessment Report of the Intergovernmental Panel on Climate Change*. Cambridge University Press.

Gibson, E. R., Hudson, P. K., & Grassian, V. H. (2006). Physicochemical properties of nitrate aerosols: Implications for the atmosphere. *The Journal of Physical Chemistry*, *110*(42), 11785-11799. https://doi.org/10.1021/jp063821k

Hansen, J., Sato, M., & Ruedy, R. (1997). Radiative forcing and climate response. *Journal of Geophysical Research: Atmospheres*, *102*(D6), 6831-6864. https://doi.org/10.1029/96JD03436

Holben, B. N., Eck, T. F., Slutsker, I. A., Tanre, D., Buis, J. P., Setzer, A., et al. (1998). AERONET - A federated instrument network and data archive for aerosol characterization. *Remote Sensing of Environment, 66*(1), 1-16. https://doi.org/10.1016/S0034-4257(98)00031-5

Johnson, B. T., Shine, K. P., & Forster, P. M. (2004). The semi-direct aerosol effect: Impact of absorbing aerosols on marine stratocumulus. *Quarterly Journal of the Royal Meteorological Society*, *130*(599), 1407-1422. https://doi.org/10.1256/qj.03.61

Kiehl, J. T., & Briegleb, B. P. (1993). The relative roles of sulfate aerosols and greenhouse gases in climate forcing. *Science*, *260*(5106), 311-314. https://doi.org/10.1126/science.260.5106.311

Koch, D., & Del Genio, A. D. (2010). Black carbon semi-direct effects on cloud cover: Review and synthesis. *Atmospheric Chemistry and Physics*, *10*(16), 7685-7696. https://doi.org/10.5194/acp-10-7685-2010

Liu, H. J., Yan, Y., Chang, H., Chen, H. Y., Liang, L. J., Liu, X. X., et al. (2019). Magnetic signatures of natural and anthropogenic sources of urban dust aerosol. *Atmospheric Chemistry and Physics*, *19*, 731-745. https://doi.org/10.5194/acp-19-731-2019

Liu, X. Y. (2000). Heterogeneous nucleation or homogeneous nucleation? *The Journal of Chemical Physics*, *112*(22), 9949-9955. https://doi.org/10.1063/1.481644

Mallet, M., Nabat, P., Johnson, B., Michou, M., Haywood, J. M., Chen, C., & Dubovik, O. (2021). Climate models generally underrepresent the warming by Central Africa biomass-burning aerosols over the Southeast Atlantic. *Science Advances*, *7*(41). https://doi.org/10.1126/sciadv.abg9998

Menon, S., Del Genio, A. D., Koch, D., & Tselioudis, G. (2002). GCM simulations of the aerosol indirect effect: sensitivity to cloud parameterization and aerosol burden. *Journal of the Atmospheric Sciences*, *59*(3), 692-713. https://doi.org/10.1175/1520-0469(2002)059<0692:GSOTAI>2.0.CO;2

Nicodemus, F. E. (1963). Radiance. *American Journal of Physics*, *31*(5), 368-377. https://doi.org/10.1119/1.1969512

Oxtoby, D. W. (1992). Homogeneous nucleation: Theory and experiment. *Journal of Physics: Condensed Matter*, *4*(38), 7627-7650. https://doi.org/10.1063/1.466859

Pistone, K., Redemann, J., Doherty, S., Zuidema, P., Burton, S., Cairns, B., et al. (2019). Intercomparison of biomass burning aerosol optical properties from in situ and remote-sensing instruments in ORACLES-2016. *Atmospheric Chemistry and Physics*, *19*, 9181-9208. https://doi.org/10.5194/acp-19-9181-2019

Pósfai, M., Gelencsér, A., Simonics, R., Arató, K., Li, J., Hobbs, P. V., & Buseck, P. R. (2004). Atmospheric tar balls: Particles from biomass and biofuel burning. *Journal of Geophysical Research: Atmospheres*, *109*(D6). https://doi.org/10.1029/2003JD004169

Redemann, J., Wood, R., Zuidema, P., Doherty, S. J., Luna, B., LeBlanc, S. E., et al. (2021). An overview of the ORACLES (ObseRvations of Aerosols above CLouds and their intEractionS) project: Aerosol–cloud–radiation interactions in the Southeast Atlantic basin. *Atmospheric Chemistry and Physics*, *21*, 1507-1563. https://doi.org/10.5194/acp-21-1507-2021

Russell, P. B., Bergstrom, R. W., Shinozuka, Y., Clarke, A. D., DeCarlo, P. F., Jimenez, J. L., et al. (2010). Absorption Angstrom Exponent in AERONET and related data as an indicator of aerosol composition. *Atmospheric Chemistry and Physics*, *10*, 1155-1169. https://doi.org/10.5194/acp-21-1507-2021

Russell, P. B., Redemann, J., Schmid, B., Bergstrom, R. W., Livingston, J. M., McIntosh, D. M., et al. (2002). Comparison of aerosol single scattering albedos derived by diverse techniques in two North Atlantic experiments. *Journal of the atmospheric sciences*, *59*(3), 609-619.

Sakaeda, N., Wood, R., & Rasch, P. J. (2011). Direct and semidirect aerosol effects of southern African biomass burning aerosol. *Journal of Geophysical Research: Atmospheres*, *116*(D12). https://doi.org/10.1029/2010JD015540

Souprayen, C., Garnier, A., Hertzog, A., Hauchecorne, A., & Porteneuve, J. (1999). Rayleigh–Mie doppler wind lidar for atmospheric measurements, I: Instrumental setup, validation, and first climatological results. *Applied Optics*, *38*(12), 2410-2421. https://doi.org/10.1364/AO.38.002410

Stier, P., Seinfeld, J. H., Kinne, S., Feichter, J., & Boucher, O. (2006). Impact of nonabsorbing anthropogenic aerosols on clear-sky atmospheric absorption. *Journal of Geophysical Research: Atmospheres*, *111*(D18). https://doi.org/10.1029/2006JD007147

Tang, I. N., Tridico, A. C., & Fung, K. H. (1997). Thermodynamic and optical properties of sea salt aerosols. *Journal of Geophysical Research: Atmospheres*, *102*(D19), 23269-23275. https://doi.org/10.1029/97JD01806

Twomey, S. (1974). Pollution and the planetary albedo. *Atmospheric Environment*, *8*(12), 1251-1256. https://doi.org/10.1016/0004-6981(74)90004-3

van der Werf, G. R., Randerson, J. T., Giglio, L., Collatz, G. J., Mu, M., Kasibhatla, P. S., et al. (2010). Global fire emissions and the contribution of deforestation, savanna, forest, agricultural, and peat fires (1997–2009). *Atmospheric Chemistry and Physics*, *10*(23), 11707-11735. https://doi.org/10.5194/acp-10-11707-2010

Wilcox, E. M. (2012). Direct and semi-direct radiative forcing of smoke aerosols over clouds. *Atmospheric Chemistry and Physics*, *12*, 139-149. https://doi.org/10.5194/acp-12-139-2012

Yu, H., Kaufman, Y. J., Chin, M., Feingold, G., Remer, L. A., Anderson, T. L., et al. (2006). A review of measurement-based assessments of the aerosol direct radiative effect and forcing. *Atmospheric Chemistry and Physics*, *6*(3), 613-666. https://doi.org/10.5194/acp-6-613-2006

Zelinka, M. D., Andrews, T., Forster, P. M., & Taylor, K. E. (2014). Quantifying components of aerosol-cloud-radiation interactions in climate models. *Journal of Geophysical Research: Atmospheres*, *119*(12), 7599-7615. https://doi.org/10.1002/2014JD021710

Zhu, J., Crozier, P. A., & Anderson, J. R. (2013). Characterization of light-absorbing carbon particles at three altitudes in East Asian outflow by transmission electron microscopy. *Atmospheric Chemistry and Physics*, *12*, 6359-6371. https://doi.org/10.5194/acp-13-6359-2013

Zuidema, P., Redemann, J., Haywood, J., Wood, R., Piketh, S., Hipondoka, M., & Formenti, P. Smoke and clouds above the Southeast Atlantic: Upcoming field campaigns probe absorbing aerosol's impact on climate. *Bulletin of the American Meteorological Society*, *92*(2), 183-201. https://doi.org/10.1175/BAMS-D-15-00082.1